Astron. Astrophys. 361, 303–320 (2000)

ASTRONOMY AND ASTROPHYSICS

Origin of H I clouds in the Local Bubble

I. A hydromagnetic Rayleigh-Taylor instability caused by the interaction between the Loop I and the Local Bubble⋆

D. Breitschwerdt⋆⋆, M.J. Freyberg, and R. Egger

Max-Planck-Institut für Extraterrestrische Physik, Giessenbachstrasse 1, 85740 Garching, Germany (breitsch,mjf,roe@mpe.mpg.de)

Received 4 January 1999 / Accepted 4 July 2000

Abstract. We present a model to explain the origin of local clouds, including the so-called Local Fluff surrounding the solar system. We present observational evidence from ROSAT PSPC data, that manifest the existence of an interaction shell between our local interstellar bubble and the adjacent Loop I superbubble. A linear stability analysis of this compressed interaction shell has been performed. We show that due to the overpressure in Loop I, a hydromagnetic Rayleigh-Taylor instability will operate, even in the presence of an obstructing and stabilizing tangential magnetic field. The field acts like surface tension in an ordinary fluid, thus inhibiting the growth of the smallest wavelengths. It is shown that the most unstable mode has a growth time of the order of $\sim 10^5$–10^6 years (depending on the magnetic field strength), in agreement with the interaction time between the two bubbles being several times longer. The wavelength of the fastest growing mode is of the order of the thickness $\delta R_{\rm sh}$ of the interaction shell (5–10 pc), or smaller depending on (i) the field strength, (ii) the angle α between the wave vector of the perturbations and and the direction of the unperturbed magnetic field, and (iii) the pressure gradient across the shell. Once the instability becomes fully non-linear, neutral blobs of size $\lesssim \delta R_{\rm sh}$ are predicted to detach from the interaction shell, aided by magnetic reconnection, and travel ballistically towards the direction of the Sun. We are thus able to identify the local clouds with products of such instabilities. Our calculations show that we can best reproduce the observed characteristics of the Local Fluff (e.g. its radius, mass, temperature, density and velocity with respect to the Sun), for a range of typical parameters of field strength 5–7 μG, density 2–3 $\rm cm^{-3}$ in the interaction shell and a perturbation angle $\alpha = 45$–$60°$.

We have also analyzed ROSAT PSPC data to show that there is a corresponding depression of absorbing HI column density in the region where the bubbles interact and the blobs detach. Moreover it is shown that this is accompanied by spectral variations in the ROSAT R1 and R2 bands, which indicate depressions or holes in the interaction region between the two bubbles.

Key words: instabilities – Magnetohydrodynamics (MHD) – ISM: bubbles – ISM: clouds – ISM: magnetic fields – X-rays: ISM

1. Introduction

The solar system is embedded in a partially ionized cloud, conventionally called the Local Cloud, Local Fluff or Local Interstellar Cloud (LIC), which is the most local patch of interstellar medium (ISM). Absorption line studies show, that in the neighbourhood of the LIC there are also other cloudlets of comparable size like e.g. the G-cloud (cf. Lallement 1998, and references therein). The state of the LIC plasma is known within some uncertainty. From GHRS measurements onboard HST its temperature is inferred to be about $7000 \pm 900\,\rm K$ (Linsky 1996). For the G cloud it could be even lower. The density inferred from line ratios, such as MgII/MgI, ranges from $n_{\rm e} = 0.3\,\rm cm^{-3}$ (Lallement et al. 1994) to $n_{\rm e} = 0.05\,\rm cm^{-3}$, for NaI (Lallement & Ferlet 1997), along different lines of sight. Using a Doppler triangulation method, the LIC velocity vector in space could be determined, having a magnitude of about $26\,\rm km\,s^{-1}$ (s. Lallement 1998), in agreement with in situ measurements of neutral helium from Ulysses (Witte et al. 1996). It is noteworthy, that for the G-cloud a value of $29\,\rm km\,s^{-1}$ (s. Lallement 1998) has been inferred, and that for both clouds the velocity vector points away from the wall or Sco-Cen direction.

As we will show in some detail in this paper, the origin of the local clouds is intimately related to the origin of the local X-ray emitting cavity, called the Local Bubble, itself. There are currently several models concerning this issue. In this respect it should be emphasized that the pressure of the LIC is $P/k_{\rm B} \sim 2000\,\rm cm^{-3}\,K$, where $k_{\rm B}$ is Boltzmann's constant, and hence at least a factor of 4–5 lower than the Local Hot Bubble model predicts (e.g. Snowden et al. 1990) for the local soft X-ray emitting plasma on the basis of collisional ionization equilibrium (CIE). However, the pressure of the LIC is in agreement with the pressure of the Local Bubble as derived from non-CIE models (Breitschwerdt & Schmutzler 1994).

It would be straightforward to assume that the local X-ray emitting plasma represents a normal patch of hot interstellar

Send offprint requests to: D. Breitschwerdt

⋆ Paper dedicated to the memory of Franz D. Kahn

⋆⋆ *Present address:* Department of Astrophysical Sciences, 108 Peyton Hall, Princeton University, Princeton, NJ 08544, USA (breitsch@astro.princeton.edu)

medium (HIM). Our range of sight in X-rays beyond 100 pc would then be blocked by intervening HI clouds (Jakobsen & Kahn 1986). However, both the overall sphericity of the cavity (cf. Snowden 1998) and the canonical temperature of $\sim 5 \times 10^5$ K of the HIM (McKee & Ostriker 1977), which is on the low side for Raymond & Smith (1977) CIE model fits to the soft X-ray background (SXRB), argue against it. Moreover UV absorption line studies (Fruscione et al. 1994) could not find any significant amount of interspersed HI within the Local Bubble. At an average radius of 100 pc, however, there is a significant increase in the HI column density indicating the presence of a swept-up shell.

The most plausible model in our view is that the Local Bubble has been created by a number of successive supernovae, presumably 10^7 or more years ago. Although there is some disagreement whether the X-ray emission is due to the reheating of the plasma by a recent supernova (e.g. Cox & Anderson 1982) or whether it is due to the slowly recombining gas of an extinct superbubble (Innes & Hartquist 1984; Smith & Cox 1998), it is suggestive that the Local Bubble is an individual object.

This is challenged in an alternative scenario by Frisch (1995, 1996), who has pictured the Local Bubble to be an appendix of the Loop I superbubble which expanded into a low density interarm region, an idea that had been proposed earlier by Bochkarev (1987). Such an expansion may have been caused by an epoch of star formation in the Sco-Cen association some 4×10^6 years ago, and the local clouds surrounding the solar system would just be fragments of the expanding shell. Based on absorption line studies within 50 pc of the Sun, it is argued that the local ISM flow has velocities in the range of $\sim 20\,\mathrm{km\,s^{-1}}$ and that the velocity vector is pointing away from Sco-Cen. It is however difficult to explain the existence of a neutral HI wall[1] between the Local Bubble and Loop I at a distance of 40 ± 25 pc in the Sco-Cen direction, which was inferred from ROSAT WFC star counts (Warwick et al. 1993) and optical and UV spectral analysis of stars in Loop I (Centurion & Vladilo 1991). The latter is still consistent with a later analysis of ROSAT EUV observations by Diamond et al. (1995), who place the rise in column density ($N_\mathrm{H} > 10^{20}\,\mathrm{cm^{-2}}$) towards the Galactic centre direction at a distance of 25–30 pc. As we will show in Sect. 4 the rise in column density to $N_\mathrm{H} \sim 10^{20}\,\mathrm{cm^{-2}}$ occurs at a distance of $\gtrsim 60$ pc using recent HIPPARCOS distances (see Fig. 9). Thus a third epoch of star formation has been postulated and the wall has been identified with the swept-up shell resulting from these explosions. The problem is then somehow shifted towards explaining how supernova remnants (SNRs) expanding into a hot low density medium can produce a neutral shell. Contrary to this view one would expect in this case that the shock wave weakens rapidly due to the high speed of sound in the medium it is propagating into, and the compression of a swept-up, expanding shell is weak. Therefore the cooling time is very large and the formation of a dense neutral shell is severely inhibited.

The North Polar Spur and its associated Loop I bubble with an huge apparent size covering a solid angle of $\sim \frac{7}{6}\pi$ on the sky have been studied in detail with the ROSAT PSPC instrument by Egger (1993) and Egger & Aschenbach (1995, henceforth EA95), using diffuse X-ray background maps of the ROSAT All-Sky Survey. Owing to its low instrumental background and high spatial resolution the PSPC is ideal for investigating the hot gas produced by supernova (SN) explosions in the nearby Sco-Cen association. It was shown (i) that the Loop I is still an active superbubble with ~ 40 SNe having already occurred and another ~ 40 to come, (ii) that the dense neutral HI shell found to be surrounding Loop I casts deep X-ray shadows in the $1/4$ keV band, (iii) that a ring-like structure ("ring") with an even higher HI column density is located between Loop I and the Local Bubble, indicated by its strong 21 cm line emission and a strong anticorrelation with the ROSAT $1/4$ keV band. By comparing these findings to numerical simulations of colliding bubbles (Yoshioka & Ikeuchi 1990), Egger (1993) concluded that the shell and ring structures were the result of an ongoing interaction between Loop I and the Local Bubble, with at least one bubble having already formed a dense and cool shell prior to the collision. In this picture the "wall" is just part of the interaction zone, held under pressure by the two colliding bubbles, and bounded by the ring. In the following we will adopt this model, because it can explain present observations in a consistent and physical way.

The purpose of this paper is to show that the existence of neutral clouds and their predominant flow away from the Sco-Cen association, is a natural consequence of the interaction between the bubbles and subsequent local fragmentation of the interaction zone (Fig. 1). The structure of the paper is as follows: Sect. 2 gives a detailed discussion of the interaction process and a thorough treatment of the resulting hydromagnetic Rayleigh-Taylor instability, in Sect. 3 the formation and dynamics of clouds is investigated and in Sect. 4 we compare the results of our calculations to ROSAT observations. Sect. 5 contains the discussion and our conclusions.

2. Interaction between Loop I and the Local Bubble

Irrespective of the detailed knowledge of the plasma state both in the Loop I and the Local Bubble, it is fair to assume that due to ongoing supernova activity in Loop I its pressure will be higher than that in the Local Bubble. For simplicity we assume a plasma in collisional ionization equilibrium (CIE) in both bubbles. This is no restriction and is conservative in the sense that the pressure inside the Local Bubble might be smaller in case of non-equilibrium models (Breitschwerdt & Schmutzler 1994). When the two bubbles first merged, probably 10^6–10^7 years ago, some complicated gas dynamical processes ensued, which are sketched qualitatively in the following. The interaction started with a head-on collision of the two outer shock waves, bounding the swept-up shells of interstellar matter. The penetration of the shocks led to a mutual weakening and retardation with a tan-

[1] For the sake of clarity we will use the term "wall" to denote the interaction zone between Loop I and the Local Bubble, and "shell" to refer to the swept-up and compressed ISM surrounding individual bubbles. The "ring" is the compressed annular zone formed in the interaction region between two interstellar bubbles and bounding the wall (see Fig. 1).

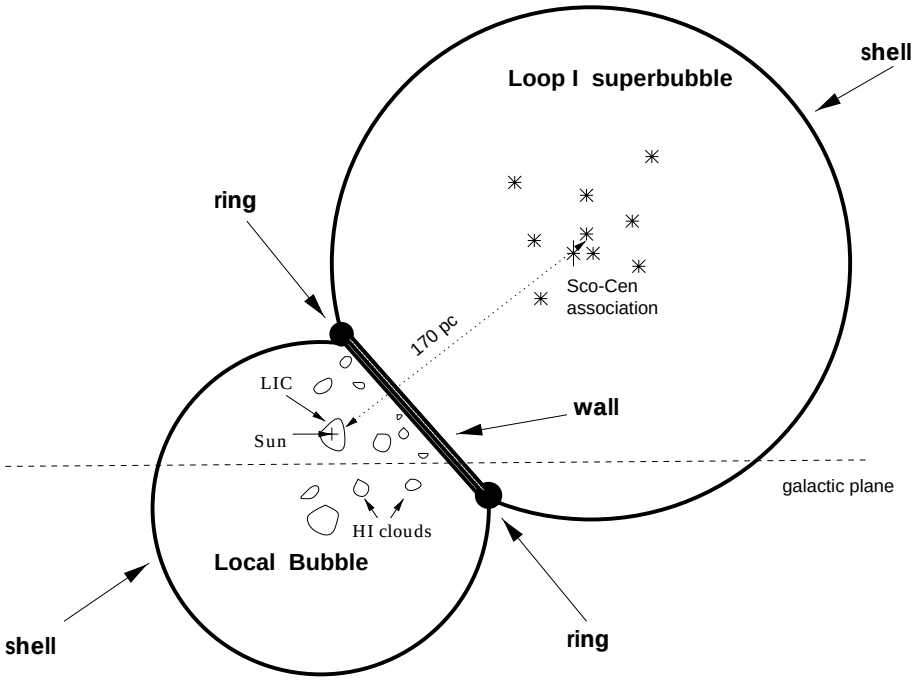

Fig. 1. Schematic representation (not drawn to scale) of the interaction between the Local Bubble and the neighbouring Loop I superbubble (longitudinal cut perpendicular to the galactic plane). The dark slab represents the dense, compressed interaction zone ("wall"), bounded by the "ring", as seen in absorption in the ROSAT images. Also shown are HI cloudlets that seem to be associated with the wall and have systematic velocities pointing towards us.

gential discontinuity occurring at the site of collision. The discontinuity separates two regions of constant pressure and flow velocity, but with different densities, temperatures and magnetic field strengths. Before an equilibrium condition could be set up, the respective shocks hit the tangential surfaces bounding each individual hot bubble, resulting in a transmitted and a reflected shock wave. The transmitted shock rapidly decays into a sound wave owing to the high speed of sound in the bubble, whereas the reflected shock interacts with the newly created tangential surface. It is well-known that such a tangential surface is unstable and will be dissolved, and the system will settle down after some time in an equilibrium configuration, characterized by a homogeneous dense interaction zone of uniform pressure and magnetic field, bounded by the tangential discontinuities of the hot bubbles on either side.

With supernova explosions in Loop I occurring on average about every 6×10^5 years (Egger 1998), the compressed shell between the two bubbles is then subject to an effective gravity $\boldsymbol{g}_{\rm eff} = (0, 0, -g_0)$ pointing towards the center of Loop I (see Fig. 2) in the rest frame of the expanding hot plasma.

Such a situation is inherently Rayleigh-Taylor unstable for all wavenumbers $|\boldsymbol{k}|$ with the largest ones growing fastest. However the presence of a magnetic field with a component parallel to $\boldsymbol{k}$ acts like surface tension in an ordinary fluid. In other words, the magnetic stresses tend to straighten out the corrugated lines of force.

The compressed wall can be represented by a thin and dense slab held under pressure from both sides. The plane parallel approach is justified, because the thickness $\delta R_{\rm sh}$ of the wall is much less than its radius of curvature[2], $R_{\rm sh}$. A stabilizing effect

[2] Due to the small relative difference in radius between the wall and the Loop I shell, we will use $\delta R_{\rm sh}$ and $R_{\rm sh}$ to denote both the wall and shell thickness and the wall and shell radius, respectively.

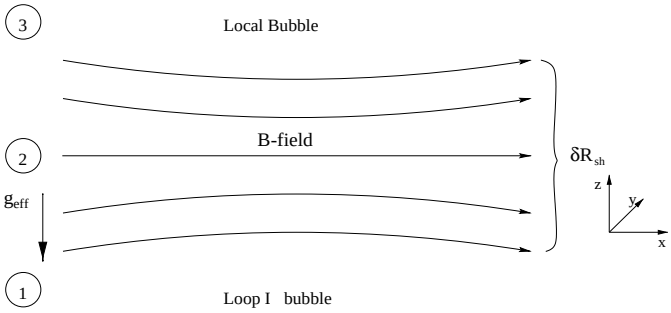

Fig. 2. Sketch of the compressed interaction zone of thickness $\delta R_{\rm sh}$ between Loop I and the Local Bubble. If the magnetic lines of force are antiparallel, magnetic reconnection will produce a neutral current sheet in which resistive dissipation occurs, thus weakening the field in the wall. The curvature of the shell boundaries is overemphasized.

due to the curvature is negligible, as has been shown in the case of the gravitational instability of a spherical shell (Tomisaka & Ikeuchi 1983). Moreover the density perturbations satisfy $\delta\varrho/\varrho \ll 1$, and the flow may therefore be considered as incompressible. In such a situation pressure and density changes can be regarded as adiabatic. In fact, the flow in an active superbubble is energy driven with occasional cooling occurring when a supernova shock wave from the interior hits the shell. The interaction zone itself is dense enough to be treated as isothermal. The sound crossing time in both the bubbles and the wall is small enough compared to the dynamical time scale for the pressure to be treated as uniform.

The hydromagnetic equations (in case of ideal MHD) to be considered are:

$$\frac{\partial \varrho}{\partial t} + \nabla\,(\varrho \boldsymbol{u}) \;=\; 0\,, \qquad (1)$$

$$\varrho\frac{\partial \boldsymbol{u}}{\partial t} + \varrho(\boldsymbol{u}\nabla)\boldsymbol{u} = -\nabla P + \frac{1}{c}(\boldsymbol{j}\times\boldsymbol{B}) + \boldsymbol{f}_{\rm ext}\,, \quad (2)$$

$$\nabla P = c_s^2\nabla\varrho\,, \quad (3)$$

$$\frac{\partial \boldsymbol{B}}{\partial t} = \nabla\times(\boldsymbol{u}\times\boldsymbol{B})\,, \quad (4)$$

$$\nabla\boldsymbol{B} = 0\,, \quad (5)$$

$$\boldsymbol{j} = \frac{c}{4\pi}(\nabla\times\boldsymbol{B})\,, \quad (6)$$

where ϱ, $\boldsymbol{u}$, P, $\boldsymbol{j}$, $\boldsymbol{B}$, $\boldsymbol{f}_{\rm ext}$, c_s and c denote the matter density, velocity, pressure, electric current density, magnetic field strength, an external force, speed of sound in the compressed interaction shell and the speed of light, respectively.

For simplicity we consider the case of $\boldsymbol{B}$ being parallel to the interface of the superbubbles and the shells, i.e. $\boldsymbol{B} = (B_0, 0, 0)$. This is also the most likely case from physical considerations, because any frozen-in magnetic field in the swept-up interstellar medium will be wrapped around the bubble as it expands. The external force will be due to the acceleration of the shell, which will described by an "effective" inwards gravitational acceleration $\boldsymbol{g}_{\rm eff}$; hence $\boldsymbol{f}_{\rm ext} = \varrho\,\boldsymbol{g}_{\rm eff}$.

2.1. The linearized perturbation equations

We make the usual ansatz for a perturbed quantity, $\boldsymbol{X} = \boldsymbol{X_0} + \delta\boldsymbol{X}$, subtract the unperturbed stationary equilibrium background state $\boldsymbol{X_0}$, and write out the components of the perturbed equations to first order. The background fluid satisfies total pressure equilibrium across the boundaries, i.e. $(d/dz)(P + B^2/8\pi) = 0$. Since the flow is dependent on z and in order to keep the treatment general, we allow for a gradient in the density and magnetic field strength.

$$\frac{\partial\delta\varrho}{\partial t} = -\delta u_z\frac{d\varrho}{dz}\,, \quad (7)$$

$$\varrho\frac{\partial\delta\boldsymbol{u}}{\partial t} = -\nabla\delta P + \frac{1}{4\pi}[(\nabla\times\delta\boldsymbol{B})\times\boldsymbol{B} + (\nabla\times\boldsymbol{B})\times\delta\boldsymbol{B}] + \delta\varrho\,\boldsymbol{g}_{\rm eff}\,, \quad (8)$$

$$\nabla\delta P = c_s^2\nabla\delta\varrho\,, \quad (9)$$

$$\frac{\partial\delta\boldsymbol{B}}{\partial t} = B_0(z)\frac{\partial\delta\boldsymbol{u}}{\partial x} - \frac{dB_0}{dz}\delta u_z\boldsymbol{e_x}\,, \quad (10)$$

$$\nabla\delta\boldsymbol{B} = 0\,, \quad (11)$$

$$\nabla\delta\boldsymbol{u} = 0\,. \quad (12)$$

Writing out Eq. (8) in components gives

$$\varrho\frac{\partial\delta u_x}{\partial t} = -\frac{\partial\delta P}{\partial x} + \frac{\delta B_z}{4\pi}\frac{dB_0}{dz}\,, \quad (13)$$

$$\varrho\frac{\partial\delta u_y}{\partial t} = -\frac{\partial\delta P}{\partial y} + \frac{B_0}{4\pi}\left(\frac{\partial\delta B_y}{\partial x} - \frac{\partial\delta B_x}{\partial y}\right)\,, \quad (14)$$

$$\varrho\frac{\partial\delta u_z}{\partial t} = -\frac{\partial\delta P}{\partial z} + \frac{B_0}{4\pi}\left(\frac{\partial\delta B_z}{\partial x} - \frac{\partial\delta B_x}{\partial z}\right) - \frac{\delta B_x}{4\pi}\frac{dB_0}{dz} - g_0\,\delta\varrho\,. \quad (15)$$

We begin by considering linear perturbations (normal modes) varying as

$$\delta\boldsymbol{X} \sim \exp[i(k_x x + k_y y) + \omega t]\,, \quad (16)$$

and propagating along the interface, where $\delta\boldsymbol{X}$ is the increment of any perturbed quantity, and

$$\boldsymbol{k} = \begin{pmatrix} k_x \\ k_y \\ k_z \end{pmatrix}\,, \qquad \boldsymbol{r} = \begin{pmatrix} x \\ y \\ z \end{pmatrix} \quad (17)$$

are the respective components of the wave vector and the distance from the origin of the coordinate frame (see Fig. 2). In the above definition for perturbations, instability will arise for ω real and positive. Using Eq. (16) one obtains the following set of equations

$$\omega\delta\varrho = -\delta u_z\frac{d\varrho}{dz} \quad (18)$$

$$\varrho\omega\delta u_x = -ik_x\delta P + \frac{\delta B_z}{4\pi}\frac{dB_0}{dz} \quad (19)$$

$$\varrho\omega\delta u_y = -ik_y\delta P + \frac{B_0}{4\pi}\,(ik_x\delta B_y - ik_y\delta B_x) \quad (20)$$

$$\varrho\omega\delta u_z = -\frac{d\delta P}{dz} + \frac{B_0}{4\pi}\left(ik_x\delta B_z - \frac{d}{dz}\delta B_x\right) - \frac{\delta B_x}{4\pi}\frac{dB_0}{dz} - g_0\delta\varrho \quad (21)$$

$$\frac{d\delta P}{dz} = c_s^2\frac{d\delta\varrho}{dz} \quad (22)$$

$$\delta\boldsymbol{B} = \frac{iB_0}{\omega}k_x\delta\boldsymbol{u} - \frac{dB_0}{dz}\frac{\delta u_z}{\omega}\boldsymbol{e_x}\,. \quad (23)$$

Making use of the incompressibility of the flow we obtain

$$\frac{d\delta u_z}{dz} = -ik_x\delta u_x - ik_y\delta u_y\,. \quad (24)$$

As usually, the above equations can be combined and rearranged so that all perturbation variables can be eliminated in favour of δu_z. Rewriting Eqs. (20) and (21) with Eqs. (18) and (23) results in

$$\varrho\delta u_y - \frac{ik_x}{\omega}\frac{B_0^2}{4\pi}\,(ik_x\delta u_y - ik_y\delta u_x) = -ik_y\left(\delta P - \frac{B_0}{4\pi\omega}\frac{dB_0}{dz}\delta u_z\right) \quad (25)$$

and

$$\varrho\delta u_z - \frac{ik_x}{\omega}\frac{B_0^2}{4\pi}\left(ik_x\delta u_z - \frac{d}{dz}\delta u_x\right) + \frac{d\delta P}{dz} - \frac{g_0}{\omega}\delta u_z\frac{d\varrho}{dz} = \frac{1}{4\pi\omega}\delta u_z\left(\frac{dB_0}{dz}\right)^2 + \frac{B_0}{4\pi\omega}\left[\frac{dB_0}{dz}\frac{d\delta u_z}{dz} + \delta u_z\frac{d^2B_0}{dz^2} - ik_x\delta u_x\frac{dB_0}{dz}\right]\,. \quad (26)$$

Next we multiply Eq. (25) with ik_x and Eq. (19) with $-ik_y$ and add them up to give

$$\varrho\omega(ik_x\delta u_y - ik_y\delta u_x) + \frac{B_0^2}{4\pi}\frac{k_x^2}{\omega}(ik_x\delta u_y - ik_y\delta u_x) = 0\,. \quad (27)$$

Therefore the term in brackets has to vanish, which is equivalent to the z-component of the vorticity, $[\nabla \times \delta\boldsymbol{u}]_z$, to be zero, i.e.

$$\delta u_y = \frac{k_y}{k_x}\delta u_x \,. \tag{28}$$

Thus Eq. (25) simply reads:

$$\varrho\delta u_y = -ik_y\left(\delta P - \frac{B_0}{4\pi\omega}\frac{dB_0}{dz}\delta u_z\right) \,. \tag{29}$$

Combining Eq. (29) with (19), using (24) and defining $k^2 := k_x^2 + k_y^2$, we obtain

$$\varrho\omega\frac{d}{dz}\delta u_z = -k^2\left(\delta P - \frac{B_0}{4\pi\omega}\frac{dB_0}{dz}\delta u_z\right) \tag{30}$$

Finally, we can use Eq. (30) to eliminate δP from (26) and after some algebra arrive at

$$\frac{d}{dz}\left(\varrho\frac{d}{dz}\delta u_z\right) - k^2\varrho\delta u_z + \frac{g_0k^2}{\omega^2}\frac{d\varrho}{dz} = \tag{31}$$
$$-\frac{k_x^2B_0^2}{4\pi\omega^2}\left[\left(\frac{d^2}{dz^2}-k^2\right)\delta u_z + \frac{1}{B_0}\frac{dB_0}{dz}\frac{d\delta u_z}{dz} + \frac{\delta u_z}{B_0}\frac{d^2B_0}{dz^2}\right] .$$

Eq. (31) will be examined now in some detail.

Disturbances with $k_x = 0$ will not cause any stretching and bending of field lines, because the wave front is coplanar to $\boldsymbol{B}$. Eq. (31) then reduces to

$$\frac{d}{dz}\left(\varrho\frac{d}{dz}\delta u_z\right) - k^2\varrho\delta u_z = -\frac{g_0k^2}{\omega^2}\frac{d\varrho}{dz} \,, \tag{32}$$

which leads to the dispersion relation of the ordinary Rayleigh-Taylor instability without magnetic field. Before discussing this special case, Eq. (31) will be solved for the general case including $\boldsymbol{B}$.

Since ϱ and $\boldsymbol{B}$ are constant in each region with a discontinuous jump across the boundary Eq. (31) reduces to

$$\varrho\frac{d^2}{dz^2}\delta u_z + \frac{k_x^2B_0^2}{4\pi\omega^2}\left(\frac{d^2}{dz^2}-k^2\right)\delta u_z - k^2\varrho\delta u_z = 0 \,, \tag{33}$$

for regions 1, 2 and 3, respectively (see Fig. 2). Across the boundaries, the solutions have to be matched, fulfilling the conditions of continuity of the velocity z-component and total pressure, i.e.

(i) $\delta u_{z,j} = \delta u_{z,j+1}$

(ii) $\delta P_j + \frac{B_{0,j}}{4\pi}\,\delta\, B_{x,j} = \delta P_{j+1} + \frac{B_{0,j+1}}{4\pi}\,\delta\, B_{x,j+1} \,,$

for $j = 1, 2$. We note, that waves propagating along the tangential discontinuities will deform the boundaries so that the gas at different positions will experience a different gravitational acceleration, which has to be included in condition (ii).

Defining the Alfvén velocity in each region by

$$v_{A,j}^2 = \frac{B_{0,j}^2}{4\pi\varrho_j} \,, \tag{34}$$

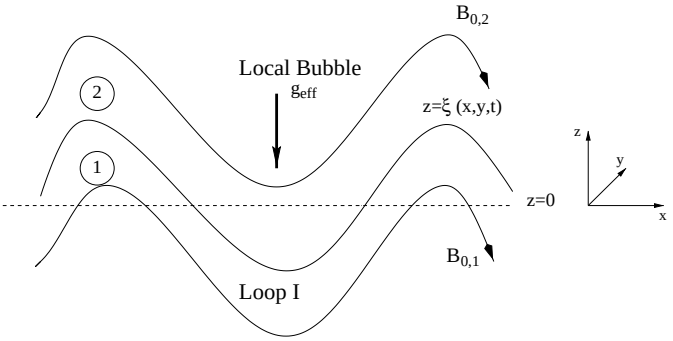

Fig. 3. Sketch of the tangential boundary between Loop I and the Local Bubble. The magnetic field is different, but constant on either side. The gravitational pull due to the weight of the fluid is a function of $\xi(x, y, t)$.

Eq. (33) reads

$$\left(1 + \frac{k_x^2v_{A,j}^2}{\omega^2}\right)\left[\frac{d^2}{dz^2} - k^2\right]\delta u_{z,j} = 0. \tag{35}$$

A trivial solution corresponds to Alfvén waves, satisfying the simple dispersion relation $\omega^2 = -k_x^2v_{A,j}^2$, and propagating along the lines of force. They do not represent unstable solutions, because k_x must be real so that for $x \to \pm\infty$, the phase factor $\sim \exp[i\boldsymbol{kx}+\omega t]$ remains finite; therefore ω is imaginary, representing a purely oscillatory behaviour.

The other solution is simply given by

$$\delta u_{z,j} = A\exp(\pm kz) \tag{36}$$

and the sign has to be chosen such that $\delta u_{z,j}$ remains finite for $z \to \pm\infty$, i.e. "$-$" for $z > 0$ and "$+$" for $z < 0$. We note that for $z = 0$ and for $z = \delta R_{\rm sh}$ (with $\delta R_{\rm sh}$ being the wall thickness), condition (i) is automatically satisfied.

The velocity field $\delta\boldsymbol{u}$ can be generally decomposed into a rotational and into an irrotational part:

$$\delta\boldsymbol{u} = \boldsymbol{v} - \nabla\psi \,. \tag{37}$$

From Eq. (12) and the general form of the rotational part, $\boldsymbol{v} = \nabla\times\boldsymbol{\varpi}$, we deduce: $\nabla^2\psi = 0$, and $\delta\boldsymbol{u} = -\nabla\psi$. Remembering that $k_z = \sqrt{k_x^2 + k_y^2} \equiv k$, we obtain

$$\psi_j = C_j\exp[i(k_xx + k_yy) \pm kz + \omega t] \,, \tag{38}$$

which goes to 0 for $z \to \mp\infty$, respectively. Condition (i) is automatically satisfied, if we observe that e.g. $C_1 = -C_2$ for $z = 0$.

Waves propagating (at some angle in general) along the magnetic lines of force will undulate the tangential discontinuity boundary and stretch the B-field, thereby increasing the magnetic tension forces (cf. the second term on either side of condition (ii)). The undulated surface will have the general form (see Fig. 3):

$$z = \xi(x, y, t) \,. \tag{39}$$

Let us now have a closer look at the deformed interface between region 1 and 2. From Eq. (13) we obtain by integrating

$$-\frac{\partial\delta P_j}{\partial x} = -\varrho_j\frac{\partial}{\partial t}\frac{\partial\psi_j}{\partial x} \,, \tag{40}$$

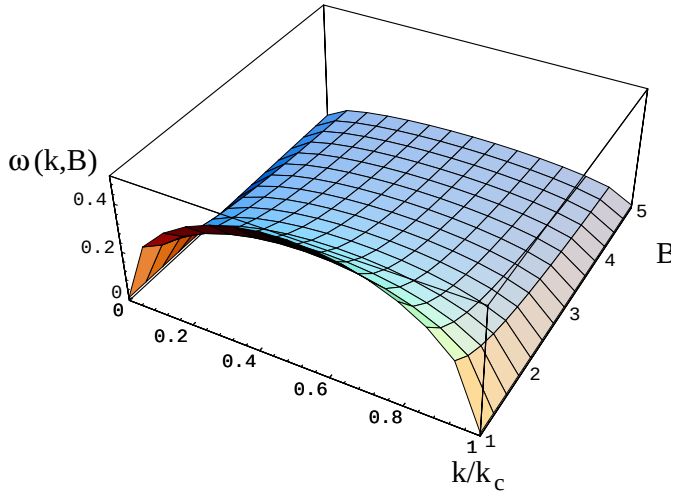

Fig. 4. The growth rate $\omega(k, |\boldsymbol{B}|)$ in arbitrary units as a function of wave vector k (in units of k_c) and magnetic field strength $|\boldsymbol{B}| = \sqrt{B_{0,1}^2 + B_{0,2}^2}$ in units of μG.

and by exchanging differentiations with respect to x and t:

$$\delta P_j = \varrho_j \omega \psi_j \,, \tag{41}$$

with $j = 1, 2$. From Eq. (23) we infer

$$\delta B_{x,j} = \frac{iB_{0,j}}{\omega} k_x \, \delta u_{x,j} = \frac{k_x^2 B_{0,j}}{\omega} \psi_j \,. \tag{42}$$

Now,

$$\delta u_{z,j} = \frac{\partial \xi}{\partial t} = -\left[\frac{\partial \psi_j}{\partial z}\right]_{z=0} = \pm k \psi_j(x, y, 0, t) \,, \tag{43}$$

and thus

$$\Longrightarrow \xi(x, y, t) = \pm \frac{k}{\omega} \psi_j(x, y, 0, t) \,. \tag{44}$$

Condition (i) therefore requires at $z = \xi$:

$$-\frac{k}{\omega} C_1 \exp[i(k_x x + k_y y) + \omega t] = \frac{k}{\omega} C_2 \exp[i(k_x x + k_y y) + \omega t] \tag{45}$$

and therefore

$$C_1 + C_2 = 0 \,, \tag{46}$$

as it was already deduced for $z = 0$.

We now inspect condition (ii). As mentioned earlier we have to incorporate the weight of the fluid between $z = 0$ and $z = \xi$, which physically corresponds to an extra accelerating force per unit area. Its value is simply given by $-g_0 \varrho_1 \xi$ in region 1 and $-g_0 \varrho_2 \xi$ in region 2. Thus condition (ii) becomes

$$\delta P_2 + B_{0,2} \frac{\delta B_{x,2}}{4\pi} = \delta P_1 + B_{0,1} \frac{\delta B_{x,1}}{4\pi} + g_0 (\varrho_2 - \varrho_1) \xi \,. \tag{47}$$

Using the expressions (41) and (42) and from (46) the relation $\psi_1 = -\psi_2$, we obtain

$$\varrho_2 \omega \psi_2 + \frac{B_{0,2}^2}{4\pi\omega} k_x^2 \psi_2 = -\varrho_1 \omega \psi_2 - \frac{B_{0,1}^2}{4\pi\omega} k_x^2 \psi_2 + g_0 \frac{k}{\omega} (\varrho_2 - \varrho_1) \psi_2 \,, \tag{48}$$

from which it follows that

$$\frac{1}{\tau_g^2} =: \omega^2 = \frac{g_0 k (\varrho_2 - \varrho_1) - \frac{k_x^2}{4\pi} \left(B_{0,1}^2 + B_{0,2}^2\right)}{\varrho_1 + \varrho_2} \,, \tag{49}$$

with τ_g being the growth time of the instability. From Fig. 4 it can be seen that the maximum growth rate occurs for $k_* = (1/2) k_c$ and that it increases with decreasing magnetic field strength (for definitions of k_c and k_* see below). Note that Eq. (49) also covers the cases of zero B-field in Loop I and the same magnitude of the field in both regions 1 and 2.

Considering our previous ansatz (16), unstable solutions must have real and positive ω. Since the density in the wall is much larger than its counterpart in the Loop I bubble ($\varrho_1 \ll \varrho_2$), this will be satisfied for any wavenumber with $0 < k < k_c$, with the critical wavenumber k_c given by

$$k_c = \frac{4\pi (\varrho_2 - \varrho_1) g_0}{\left(B_{0,1}^2 + B_{0,2}^2\right) \cos^2 \alpha} \,, \tag{50}$$

where we have used $k_x = k \cos\alpha$, with α being the angle between the wave vector of the perturbation and the direction of the undisturbed magnetic field lines. The term $-\frac{k_x^2}{4\pi} \left(B_{0,1}^2 + B_{0,2}^2\right)$ introduces an upper limit in the unstable wavenumbers. Thus magnetic tension forces have a stabilizing effect, just as surface tension in an ordinary fluid.

In the classical Rayleigh-Taylor instability (see Eq. (32)) there is no limit on k as we can see by setting $B_{0,1} = B_{0,2} = 0$, with the largest wavenumbers growing fastest. The same is true for perturbations with $\alpha = \pi/2$, which do not lead to a deformation of the field lines but simply to an exchange of higher field and lower field plasma. We believe that the present topology of field and plasma does not easily promote such a process. Firstly, we have treated for simplicity the onset of instability for slab geometry whereas, on larger scales, the field lines are circular and wrapped around the bubbles or, considering the shell, may even be rooted somewhere in the undisturbed interstellar medium. Secondly, $B_{0,1}$ and $B_{0,2}$ are in general not parallel but oblique with respect to each other, thereby also seriously inhibiting the exchange mode.

In the following, we will therefore consider the bending mode instability and take $0 \leq \alpha < \pi/2$ in our numerical estimates. In this case our simplifying assumptions on the field geometry will not cause any restrictions. The most unstable wavenumber, k_*, is given by (cf. Appendix A)

$$k_* = \frac{1}{2} k_c \,. \tag{51}$$

The corresponding growth time is then

$$\tau_g(k_*) = \sqrt{\frac{1}{\pi} \left(B_{0,1}^2 + B_{0,2}^2\right) (\varrho_1 + \varrho_2)} \, \frac{\cos\alpha}{(\varrho_2 - \varrho_1) g_0} \,. \tag{52}$$

Before discussing the implications of Eq. (52) for the interaction zone between Loop I and the Local Bubble, we have a brief look at the interface between regions 2 and 3, i.e. the tangential discontinuity between the shell and the Local Bubble. It is intuitively clear, that a stratification in which a dilute and

light fluid is gravitationally supported by a dense and heavy one is inherently stable. Shifting our coordinate system with $z = 0$ to the boundary separating regions with densities ϱ_2, ϱ_3 and field strengths $B_{0,2}$, $B_{0,3}$, respectively, we can apply the same analysis as before and find accordingly

$$\omega^2 = \frac{g_0 k(\varrho_3 - \varrho_2) - \frac{k_x^2}{4\pi}\left(B_{0,2}^2 + B_{0,3}^2\right)}{\varrho_2 + \varrho_3} \,. \tag{53}$$

Now $\varrho_3 \ll \varrho_2$, hence ω is purely imaginary and all solutions will therefore be stable.

However, once the instability becomes fully nonlinear, the whole wall separating the Local Bubble and Loop I will be affected (cf. next section).

3. The formation and dynamics of clouds

The linear stability analysis in the previous section has shown that there are perturbations of a minimum wavelength that can grow beyond any limit. However, restricting ourselves to small amplitude perturbations we cannot follow the instability into the nonlinear regime. Qualitatively we expect that the unstable waves will affect the whole wall, which will become heavily corrugated. Bending of the field lines will become so severe that magnetic reconnection will occur across antiparallel lines of force coming close to each other. Therefore the field cannot ultimately prevent fragmentation of the wall into blobs of typical diameter $d_b \sim k_*^{-1}$. Before we can calculate the size of such a cloudlet, we have to discuss the properties of Loop I and the Local Bubble, from which the pressure difference across the wall, driving the instability, can be inferred.

3.1. Properties of the Loop I superbubble

The plasma properties of the Loop I superbubble were determined by spectral analysis of ROSAT PSPC soft X-ray data along several radial cuts across the North Polar Spur (Egger 1993, 1995). Deprojection under assumption of spherical symmetry resulted in radial n- and T-profiles of the bubble. Large variations are found in density as well as in temperature, and in some regions the uncertainties are considerable. However, close to the bright edge of the Spur, i.e. the shock heated rim of the bubble, the data are relatively clear and the 1σ statistical errors only about $\pm 6\%$ (Egger 1993). To be conservative we use a value of $\pm 10\%$. Values derived from spectral fitting are generally model dependent. Here we have carefully reanalyzed the data obtained by Egger (1993) and have used the standard Raymond-Smith collisional ionization equilibrium (CIE) model with solar abundances. As a result the derived parameters for n and T are not statistically independent. Typical values of the shocked interior of the bubble close to the shell are $T_{\rm LI} = 2.5 \times 10^6\,{\rm K}$ and $n_{\rm LI} = 1.5 \times 10^{-2}\,{\rm cm}^{-3}$. To lowest order, variations in $n_{\rm LI}$ and $T_{\rm LI}$ are such that the pressure $p/(2k_{\rm B}) = n\,T$ is uniform on a global scale, except for some regions, as mentioned above. Since the errors of n and T are of the same order the maximum and minimum allowable pressure for Loop I are $p/(2k_{\rm B}) = 4.125 \times 10^4$ and $3.375 \times 10^4\,{\rm cm}^{-3}\,{\rm K}$, respectively. In the same manner we obtain for the Local Bubble from the conservative assumption of CIE $n_{\rm LB} = 5.2 \times 10^{-3}\,{\rm cm}^{-3}$ and $T_{\rm LB} = 1.2 \times 10^6\,{\rm K}$ for the density and temperature, respectively (Egger 1993). Errors are of the same order so that the maximum and minimum permissible pressure range is $p/(2k_{\rm B}) = 0.686 \times 10^4$ and $0.562 \times 10^4\,{\rm cm}^{-3}\,{\rm K}$, respectively.

From absorption measurements of soft X-rays with ROSAT it is known that the HI column density of the wall is $N_{\rm w} \approx 10^{20}\,{\rm cm}^{-2} = N_{20}\,10^{20}\,{\rm cm}^{-2}$ (Egger 1998). Thus the wall thickness is

$$\delta R_{\rm w} \sim \frac{N_{\rm w}}{n_{\rm w}} \approx 3\,\frac{N_{20}}{n_{10}}\,{\rm pc}\,, \tag{54}$$

where we have written $n_{\rm w} = n_{10}\,10\,{\rm cm}^{-3}$. Note that the column density of the wall $N_{\rm w}$ is presumably about twice that of the Loop I shell, $N_{\rm sh}$; however since the observational uncertainties of the shell thickness can be larger than a factor of 2, we do not discriminate in the following.

The pressure difference between Loop I and the Local Bubble leading to the acceleration of the wall ranges $\Delta P = 7.4 \times 10^{-12}$ to $9.8 \times 10^{-12}\,{\rm g}/({\rm cm\,s}^2)$. Thus even in the worst case there is a substantial pressure difference that pushes the wall into the Local Bubble and ensures the existence of an instability. In the following estimates we use for convenience the mean value $\Delta P \approx 8.7 \times 10^{-12}\,{\rm g}/({\rm cm\,s}^2)$.

The z-component of the "effective gravitational" acceleration of the wall is then given by

$$g_0 = \frac{\Delta P}{\bar{m} N_{\rm w}} \approx 5.8 \times 10^{-8}\,{\rm cm/s}^2\,, \tag{55}$$

with $\bar{m} \approx 2 \times 10^{-24}\,{\rm g}$ being the mean interstellar atomic mass, and $N_{\rm w} = 7.510^{19}\,{\rm cm}^{-2}$ (see Sect. 4.1).

The average radius of the Loop I bubble is $R_{\rm sh} \approx 150\,{\rm pc}$ and therefore the density of the ambient medium is (Egger 1993)

$$n_0 = \frac{3N_{\rm sh}}{R_{\rm sh}} \approx 0.5\,{\rm cm}^{-3}\,. \tag{56}$$

3.2. Properties of the unstable region

The wall and the Loop I shell are illuminated by the stellar content of the Sco-Cen association. The dynamical age of the stellar cluster is about 2×10^7 years and therefore the number of SN candidate stars is about 40 of spectral type between B3 and B1 (Egger 1993). The Lyman continuum output rate of a B1 star is $S_{\rm B1} \approx 3.3 \times 10^{45}$ photons s^{-1} (Spitzer 1978). In order to keep the wall ionized a photon rate of

$$\begin{aligned} S_* &= 4\pi\beta^{(2)} n_{\rm w}^2 R_{\rm sh}^2 \delta R_{\rm sh} \\ &= 4\pi\beta^{(2)} R_{\rm sh}^2 N_{\rm w} n_{\rm w} \\ &\approx 7.2 \times 10^{50}\,N_{20}\,n_{10} \quad {\rm photons\,s}^{-1}\,, \end{aligned} \tag{57}$$

is required, where $\beta^{(2)} = 2 \times 10^{-10}\,T^{-(3/4)}\,{\rm cm}^3/{\rm s} \approx 2.36 \times 10^{-13}\,{\rm cm}^3/{\rm s}$ for $T = 8000\,{\rm K}$ (see below) is the recombination coefficient for hydrogen into the atomic level $n = 2$, excluding recombinations into the ground state which produce an ionizing

Table 1. Temperature of the wall, $T_{\rm w}$, plasma beta β_P, Alfvén speed, $v_{\rm Aw}$, growth time of the most unstable mode, $\tau_g(k_*)$, diameter, d_b, and mass, m_b, of the clouds, respectively, as a function of magnetic field strength, B_{-6}, in the unstable region, for $\alpha = 0$, $n_{10} = 0.5$ and $N_{20} = 0.75$ (see Sect. 4.1).

Properties of blobs in the unstable region					
$B_{-6}[\mu{\rm G}]$	2	3	5	7	10
$T_{\rm w}$ [K]	8570	8280	7320	5980	3040
β_P	37	16	5.0	2.0	0.5
$v_{\rm Aw}$ [km s^{-1}]	1.7	2.5	4.2	6.0	8.5
$\tau_g(k_*)$ [yr]	$2.0\cdot10^5$	$2.9\cdot10^5$	$4.9\cdot10^5$	$6.8\cdot10^5$	$9.8\cdot10^5$
d_b [pc]	0.4	0.8	2.2	4.4	8.9
m_b [$M_\odot$]	0.003	0.04	0.8	6.2	53

photon to be absorbed "on the spot". Therefore the number of early type stars falls short by 3 orders of magnitude and the shell mainly consists of moderately warm neutral HI. The same is true for the wall, because in the Local Bubble there is no known stellar cluster that could contribute to ionization.

The magnetic field strengths inside Loop I and in the shell are largely unknown. Since Loop I was first observed as an annular structure in radio wavelengths (Berkhuijsen et al. 1971), and from spectral index and polarization measurements it became clear that the radio emission is due to synchrotron radiation, there must be a non-negligible magnetic field associated with the shell. Conversely, there is a lack of radio emission from the bubble itself, so that $|B_{0,1}|/|B_{0,2}| \ll 1$. We assume that $|B_{0,1}| = 0$ and $|B_{0,2}| = B_{-6}\mu$G, with $B_{-6} = 5$, $n_{10} = 0.5$ and $N_{20} = 0.75$ (see Sect. 4.1) as typical values. In Table 1 we have listed the properties of the interaction region as a function of B_{-6}. The temperature of the magnetized wall is then roughly given by

$$\begin{aligned} T_{\rm w} &= \frac{P_w - B_{0,2}^2/8\pi}{n_{\rm w}k_{\rm B}} \\ &= \left(\frac{4380}{n_{10}} - 28.8\frac{B_{-6}^2}{n_{10}}\right)\ [{\rm K}] \\ &\approx 7320\,{\rm K}\,, \end{aligned} \tag{58}$$

with the average pressure of the wall being $P_w = P_{\rm LB} + \frac{1}{2}\Delta P \approx 6.04\times10^{-12}\,{\rm dyne\,cm^{-2}}$, which takes into account the pressure gradient across the shell.

We know that $\varrho_1/\varrho_2 \ll 1$; hence the growth time of the fastest growing mode is given by

$$\begin{aligned} \tau_g(k_*) &= \sqrt{\frac{1}{\pi}(\varrho_1+\varrho_2)}\,\frac{B_{0,2}\cos\alpha}{(\varrho_2-\varrho_1)g_0} \\ &= \frac{B_{0,2}\cos\alpha}{g_0\sqrt{\pi\varrho_2}} \\ &= \sqrt{\frac{\bar m}{\pi n_{\rm sh}}}\,\frac{N_{\rm w}B_{0,2}\cos\alpha}{\Delta P} \\ &= 9.2\times10^4\,\frac{N_{20}B_{-6}\cos\alpha}{\sqrt{n_{10}}}\ {\rm yrs} \\ &\approx 4.9\times10^5\,{\rm yrs}\,. \end{aligned} \tag{59}$$

The instability will eat its way through the wall, steadily producing blobs of size

$$\begin{aligned} d_b &\sim 1/k_* \\ &= \frac{\left(B_{0,1}^2 + B_{0,2}^2\right)\cos^2\alpha}{2\pi\, g_0(\varrho_2-\varrho_1)} \\ &= \frac{B_{0,2}^2\cos^2\alpha N_{\rm sh}}{2\pi\,\Delta P n_{\rm sh}} \\ &= 0.06\,\frac{N_{20}B_{-6}^2\cos^2\alpha}{n_{10}}\ {\rm pc} \\ &\approx 2.2\,{\rm pc}\,. \end{aligned} \tag{60}$$

As it turns out, the size of the blobs is comparable to or less than the thickness of the interaction zone and thus fragmentation of the wall and creation of holes or depressions in neutral hydrogen column density by detachment of blobs seems very likely. This is achieved by significant mass motions induced by the fastest growing mode. The creation of blobs will be assisted by magnetic reconnection, which in case of Petschek's (1964) mechanism typically occurs at a rate $\sim 0.1\,v_{\rm Aw}/l$, where l is the typical distance between antiparallel lines of force and $v_{\rm Aw}$ is the Alfvén speed in the wall. Once the waves will become nonlinear (within a few growth times[3]) and turbulence will be fully developed, l will be sufficiently small for reconnection to proceed due to tangling and twisting of field lines.

The plasma beta is given by $\beta_P = 8\pi n_{\rm sh}k_{\rm B}T_{\rm sh}/B_{0,2}^2 = 35\,n_{10}\,(T_w/1000[K])/B_{-6}^2$; therefore the dynamics of the plasma in the shell will be largely determined by the thermal pressure as long as $B_{-6} < 10$.

3.3. Cloud dynamics

Here we consider blobs to be driven by the pressure force ΔP acting on the wall and hence also on individual blobs. Once the blobs have detached, they will move ballistically through the Local Bubble without any noticeable deceleration, because the mass of hot gas swept up by a blob is in general negligible in comparison to the mass of the blob itself. For simplicity we assume the blobs to be spherically symmetric (see discussion below).

The equation of motion is then given by

$$\begin{aligned} m_b\frac{d\boldsymbol{v_b}}{dt} &= F\boldsymbol{e_z} \\ &= \frac{\pi}{4}d_b^2\Delta P\boldsymbol{e_z}\,, \end{aligned} \tag{61}$$

where m_b and $\boldsymbol{v_b}$ denote the mass and the velocity of a blob, respectively. The mass can be written as

$$\begin{aligned} m_b &= \frac{4}{3}\pi n_{\rm sh}(d_b/2)^3 \\ &= 3.310^{-5}\,\frac{N_{20}^3\bar m B_{-6}^6\cos^6\alpha}{n_{10}^2}\ {\rm M}_\odot \\ &\approx 0.8\,{\rm M}_\odot\,. \end{aligned} \tag{62}$$

[3] There has been a recent suggestion to increase the reconnection rate by turbulence (Lazarian & Vishniac 2000), mainly due to the increase of the surface area over which antiparallel lines of force could merge.

The cloud mass is a very sensitive function of the field strength, and values of $B_{-6}\cos\alpha > 5$ are above the estimated mass of the LIC (see Table 1), which is more of the order of $\sim 1\,M_\odot$.

The acquired velocity increase Δv_b by the accelerating force over a time Δt is

$$\Delta v_b = \frac{3}{2}\frac{\Delta P \Delta t}{\bar{m} N_\mathrm{w}}\,. \tag{63}$$

Note, that if $d_b > \delta R_\mathrm{sh}$, the blobs will have a more flattened shape, and $m_b \approx \pi \bar{m}(d_b/2)^2 N_\mathrm{w} \approx 2.710^{-3}(N_{20}/n_{10})^2 B_{-6}^4 \cos^4\alpha$ and therefore $\Delta v_b = \Delta P \Delta t/\bar{m} N_\mathrm{w}$; as expected, the geometry factor in Eq. (63) is of order unity. With the values adopted for the interaction region this occurs for $B_{-6}\cos\alpha \geq 10$.

The duration of the applied force is approximately the timescale of the formation of the blob, which is a few growth times (for the instability to become fully nonlinear), i.e. $\Delta t \sim \eta\tau_g(k_*)$, where η is typically a factor of up to a few. Using Eq. (59), we obtain

$$\begin{aligned}\Delta v_b &\sim \frac{3}{2}\eta\frac{\Delta P \tau_g(k_*)}{\bar{m} N_\mathrm{w}} \\ &= 3\eta\frac{B_{0,2}\cos\alpha}{\sqrt{4\pi\bar{m} n_\mathrm{w}}} \\ &\equiv 3\eta v_\mathrm{Aw}\cos\alpha\,.\end{aligned} \tag{64}$$

Using the previous numbers, we find that $v_\mathrm{Aw} = 0.6\,(B_{-6}/\sqrt{n_{10}})\,\mathrm{km\,s^{-1}} \approx 4.2\,\mathrm{km\,s^{-1}}$ (for $\alpha = 0$) and hence $\Delta v_b \sim 12.7\eta\,\mathrm{km\,s^{-1}}$. For a reasonable value of $\eta \approx$ 2–3 it is possible, for example, to recover the observed cloud velocities of $\sim 26\,\mathrm{km\,s^{-1}}$.

The pressure in the blob, when it is generated, is subject to a gradient, which will level off after it has detached within a few sound crossing times, $\tau_\mathrm{sc} \sim 7 \times 10^3 N_{20} B_{-6}^2 \cos^2\alpha/(n_{10}^{1.5}(T_b/1000[K])^{0.5}) \approx 1.4 \times 10^5$ yrs, typically less than the growth time of the instability; in the following subscript "*b*" denotes blob quantities. The pressure is shared between the thermal, magnetic and the turbulent pressure (resulting from the instability). The magnitude of the latter is given by $\delta P \sim \frac{1}{2}\rho(\delta u)^2$, where the fluctuation amplitude δu is of the order of the Alfvén speed of the perturbed field, which is of the order of the background field or even larger in the nonlinear regime. The temperature is therefore approximately given by $T_b \approx 4380/n_{10} - 57.6 B_{-6}^2/n_{10}\,\mathrm{K}$.

After detachment from the wall the blob expands until it is in pressure equilibrium with the surrounding Local Bubble medium. Assuming conservation of mass, $\varrho V = \mathrm{const}$, and $pV = \mathrm{const}$, for isothermal expansion, we can estimate the density of the cloud, n_cl, from $n_\mathrm{cl}/n_b = (P_\mathrm{LB}/P_b)$. Here $P_b \approx P_\mathrm{LB} + \frac{1}{2}\Delta P$ is the average pressure of the blob, ranging from $(5.26\text{–}6.81) \times 10^{-12}\,\mathrm{dyne\,cm^{-2}}$, for the values derived in Sect. 3.1, $P_\mathrm{LB} = (1.55\text{–}1.9) \times 10^{-12}$ and $P_\mathrm{LI} = (7.4\text{–}9.8) \times 10^{-12}$ in their respective units. As we shall see, the size of the blobs is probably less than the thickness of the wall and therefore the average pressure of the blob may vary between $n_\mathrm{cl}/n_b = (1 + (\Delta P/P_\mathrm{LB}))^{-1}$ and $(1 + (\Delta P/(2P_\mathrm{LB})))^{-1}$, thus $n_\mathrm{cl}/n_b \approx 0.13\text{–}0.34$. Accordingly, the cloud radius after cloud expansion is estimated to be $R_\mathrm{cl}/R_\mathrm{b} = (n_\mathrm{b}/n_\mathrm{cl})^{1/3} \approx 1.4\text{–}2.0$. The cloud mass is given by Eq. (62).

For a direct comparison, we use the Local Cloud (LIC). The density of the LIC is not very well determined; values for the electron density range from $n_\mathrm{e} = 0.05$ (Lallement & Ferlet 1997) to $0.3\,\mathrm{cm^{-3}}$ (Gry et al. 1995), depending on the method used and the direction of the line of sight. To infer the gas density one has to know the degree of ionization. It has been reported by various authors (e.g. Slavin & Frisch 1998) that helium is overionized relative to hydrogen and therefore the LIC is probably not in ionization equilibrium. From the HI and HeI backscattering radiation as well as the direct measurement of HeI with *Ulysses* the most likely value for the total LIC density is $0.32\,\mathrm{cm^{-3}}$ (Frisch et al. 1999).

We obtain good agreement between observations and the model for a set of parameters: $n_{10} = 0.2\text{–}0.3$, $B_{-6} = 6\text{–}7$, $\alpha = 45\text{–}60°$ for the angle of the propagating waves with respect to the B-field (cf. Table 2). Note that the temperature of the LIC in the model is not well determined due to the variation of ΔP; the mean value is $T_\mathrm{cl} = 7740\,\mathrm{K}$, for the most probable value of $P_b = 6.0 \times 10^{-12}\,\mathrm{dyne\,cm^{-2}}$. The velocity is reproduced for a plausible range of $\eta \sim 2$ (see above). The growth time of the instability for our chosen parameters is $\tau_g(k_*) \sim 5 \times 10^5$ yrs. In Table 2 we have listed results from both the classical CIE model and a non-equilibrium ionization model of the Local Bubble (Breitschwerdt & Schmutzler 1994); the latter results in a much lower Local Bubble pressure (by a factor of 5) and hence in a somewhat larger pressure difference ΔP across the wall. One of the advantages of a non-CIE model is that the plasma in the Local Bubble is in pressure equilibrium with the Local Cloud and does therefore not put any restrictions on the cloud survival. During the travel of the cloud from its site of formation to the solar system it may be subject to processes like ablation, irradiation and heat conduction (although reduced by the magnetic field), which may modify the values derived above. To include these complications is beyond the scope of the present paper.

3.4. Deceleration of the wall

The data analysis of the Leiden-Dwingeloo Survey shows that the wall itself appears to move towards the Sun with a velocity of about $5\,\mathrm{km\,s^{-1}}$ (Freyberg et al., 2000). This is by a factor of five lower than the velocity of the local clouds. The discrepancy can be explained in the following way. Initially, when the two bubbles came into contact first, the magnetic field lines were locally straight lines (see Fig. 2). As the field was subsequently bulging into the Local Bubble due to the overpressure ΔP, magnetic tension forces began to arise. Combining Eqs. (3) and (6) we obtain for the modified Euler equation

$$\begin{aligned}\varrho\frac{d\boldsymbol{u}}{dt} &= -\nabla P + \frac{1}{4\pi}(\nabla\times\boldsymbol{B})\times\boldsymbol{B} \\ &= -\nabla\left(P + \frac{B^2}{8\pi}\right) + \frac{1}{4\pi}(\boldsymbol{B}\nabla)\boldsymbol{B}\,.\end{aligned} \tag{65}$$

Table 2. The model parameters are given for a Local Bubble model assuming collisional ionization equilibrium (CIE) and for a non-equilibrium model taken from Breitschwerdt & Schmutzler (1994; B&S), respectively (for details see Breitschwerdt 1996). A value of $N_{20} = 0.75$ was adopted for the column density of the wall throughout.

Comparison between LIC and model			
	LIC[1]	(CIE)	(B&S)
		$B_{-6} = 7, \alpha = 60^\circ$ $n_{10} = 0.2$	$B_{-6} = 6, \alpha = 45^\circ$ $n_{10} = 0.3$
$n_{\rm H}$ [cm^{-3}]	0.05–0.32[2]	0.26–0.68	0.07–0.15
$T_{\rm cl}$ [K]	7800–9700[3]	4910–21500	5770–16800
$M_{\rm cl}$ [M$_\odot$]	0.07–0.9	0.4–1.0	0.4–0.8
$R_{\rm cl}$ [pc]	$2.2 - 2.7$	1.7–3.2	2.8–4.4
$v_{\rm LSR}$ [km s^{-1}]	25.7	25.7 $\eta = 1.8$	25.7 $\eta = 1.8$

[1] data taken from Linsky & Redfield (1999)
[2] data taken from Frisch et al. (1999)
[3] data taken from Dring et al. (1997)

Whereas the magnetic pressure force $B^2/8\pi$ adds to the acceleration of the wall, this effect is more than compensated by the magnetic tension forces.

For illustration, let us consider a simple case of Eq. (65). We assume axisymmetry, and for simplicity a purely azimuthal field, $\boldsymbol{B} = (0, B_\varphi(r,z), 0)$. At $t = 0$ (when the two bubbles came into contact), we require that the radial velocity u_r, which is the deviation from the mean bubble expansion, is zero. In this initial phase, the nonlinear terms $(\boldsymbol{u}\nabla)\boldsymbol{u}$, which are of second order, will be small compared to $\partial\boldsymbol{u}/\partial t$. We then have

$$\varrho\frac{\partial u_r}{\partial t} = -\frac{\partial}{\partial r}\left(P + \frac{B^2}{8\pi}\right) - \frac{B^2}{4\pi r} \tag{66}$$

$$\varrho\frac{\partial u_z}{\partial t} = -\frac{\partial}{\partial z}\left(P + \frac{B^2}{8\pi}\right) . \tag{67}$$

In this idealized setup, the longitudinal flow velocity u_z is small. We are primarily interested in the time dependence of the radial flow. Therefore integration of Eq. (67) yields

$$P + \frac{B^2}{8\pi} = -F(r) , \tag{68}$$

where $F(r)$ is an arbitrary function of r; the "$-$" sign accounts for the fact that the negative gradient of the left-hand side gives a positive acceleration. The acceleration of the radial component then becomes

$$\varrho\frac{\partial u_r}{\partial t} = F'(r) - \frac{B^2(r,t)}{4\pi r} , \tag{69}$$

and upon integration with respect to time gives

$$u_r(r,t) = F'(r)t - \frac{1}{4\pi r}\int_0^t B^2(r,t')dt' , \tag{70}$$

which satisfies the boundary condition. Eq. (70) shows, that as the field lines bulge into the Local Bubble, and the radius of curvature of the lines of force becomes smaller, the magnetic tension decelerates the wall.

Once the blobs have detached from the wall after $\Delta t = \eta\tau_g$, they will therefore travel ahead. Whether the wall will eventually stall, depends on the interplay between pressure and tension forces. However, on general grounds it is unlikely that an equilibrium configuration of such a kind does exist in three dimensions.

3.5. Can the clouds be accelerated by outflowing gas of Loop I?

We may also speculate, whether the clouds might be accelerated due to the blow-out of gas from Loop I through the holes, which are caused by the detachment of the blobs. There is no guarantee that such a mechanism might work here, and we merely mention it as an interesting possibility.

Suppose that the holes in the wall form an idealized convergent-divergent device, known as a de Laval nozzle. In Loop I, the gas flows subsonically towards the holes, becomes sonic at the throat and supersonic when it enters the Local Bubble. At the blob surface there will exist a stagnation point, and a bow shock will decelerate the supersonically impinging gas flow, thus converting part of the kinetic into thermal energy. In the following estimates we will neglect these details, because the overall effect on the blob will be acceleration, although the post-shock gas will be deflected sideways and only part of the incoming kinetic energy can be transferred to the cloud.

The force per unit area acting on the cloud due to the jet of plasma channelled through a hole is the difference between its ram pressure and the thermal pressure in the Local Bubble; hence

$$m_b\frac{d\boldsymbol{v_b}}{dt} = \frac{\pi}{4}d_b^2\left(\varrho_j v_j^2 - P_{\rm LB}\right)\boldsymbol{e_z} , \tag{71}$$

where v_j, ϱ_j are the velocity and density of the jet, respectively. Essentially, thermal pressure in Loop I at the base of the jet is converted into kinetic energy. The maximum effect is reached if the efficiency is 100%. In this case we obtain from Bernoulli's equation

$$v_j \sim \sqrt{\frac{2\gamma_g}{\gamma_g - 1}\frac{P_{\rm LI}}{\varrho_{\rm LI}}} = \sqrt{\frac{2}{\gamma_g - 1}}\, c_{\rm LI} , \tag{72}$$

where $c_{\rm LI}$ is the speed of sound in Loop I. Thus, assuming $\gamma_g = 5/3$, and using $P_{\rm LB} \approx 1/5\,\Delta P$ for the values discussed in Sect. 3.1, we obtain

$$\Delta v_b \simeq 9.0\frac{\Delta P \Delta t}{\bar{m} N_{\rm w}} , \tag{73}$$

where for simplicity $d_b \sim \delta R_{\rm sh}$ has been assumed. This acceleration could be quite substantial if compared to Eq. (63); the question is: what is Δt in here? A steady jet will expand freely for a time

$$t_{\rm exp} = \int_0^L \frac{dz}{v_j} , \tag{74}$$

where L is the distance in z-direction from the hole. Therefore $\sqrt{(\gamma_g-1)/2}\,L_j/c_{\rm LI} < t_{\rm exp} < L_j/c_{\rm LI}$, with L_j being the maximum distance of free expansion. We don't know how well collimated the jet will be; it is supposed to have a half opening angle θ with respect to the z-axis, with $\tan\theta = dr/dz$, where r is the radial coordinate. Its Mach number increases along the z-axis, and appreciable deceleration will occur at a distance L_j, where it has roughly swept up its own mass:

$$\dot{m}\, t_{\rm exp} \sim \varrho_{\rm LB} V_j\,, \tag{75}$$

where V_j is the volume of the conical jet and $\dot{m}$ is the mass flux through the hole. In order to evaluate $\dot{m}$ we use the equation of continuity and Bernoulli's equation for a polytropic gas; since there is no significant exchange of heat between the jet and the surrounding medium we use the adiabatic law $P = C\varrho^{\gamma_g}$ where C is a constant depending on the specific entropy of the gas.

$$\varrho v A \;=\; const. \tag{76}$$

$$\frac{1}{2}v^2 + \frac{c^2}{\gamma_g - 1} \;=\; D\,, \tag{77}$$

with D being constant along a streamline. At the critical point of the flow Eq. (77) becomes (Courant & Friedrichs 1948)

$$\frac{\gamma_g - 1}{\gamma_g + 1}v^2 + \frac{2c^2}{\gamma_g + 1} = c_*^2\,, \tag{78}$$

where c_* is the speed of sound at the critical point in the flow. With increasing distance from the jet the speed of sound drops and the fluid velocity increases, so that we obtain from Eq. (78) approximately

$$v_j^2 \approx \frac{\gamma_g + 1}{\gamma_g - 1}c_*^2 \quad \Rightarrow c_*^2 = \frac{2c_{\rm LI}^2}{\gamma_g + 1}\,. \tag{79}$$

Using the adiabatic law and Eq. (78), the mass flux into the jet is given by

$$\begin{aligned}\dot{m} \;&=\; \varrho_* c_* A_* \\ &=\; \varrho_{\rm LI} c_{\rm LI} A_* \left(\frac{2}{\gamma_g + 1}\right)^{\frac{\gamma_g+1}{2(\gamma_g-1)}} \qquad (80)\\ &\approx\; 0.6\pi\varrho_{\rm LI} c_{\rm LI}\frac{d_b^2}{4}\,, \qquad (81)\end{aligned}$$

where the diameter of the surface area A_* at the throat of the nozzle has been equated to the diameter of the clouds. For a proper jet we expect $d_b/2L_j \ll 1$, and therefore

$$V_j \approx \frac{1}{3}\pi L_j^2\left(L_j\tan^2\theta + \frac{3}{2}d_b\tan\theta\right)\,. \tag{82}$$

Using the minimum expansion time, $t_{\rm exp} = L_j/v_j = \sqrt{(\gamma_g-1)/2}\,L_j/c_{\rm LI}$, Eq. (75) yields

$$L_j \;=\; \frac{3d_b}{4\tan\theta}\left[\sqrt{1 + \frac{4}{3\sqrt{3}}\frac{\varrho_{\rm LI}}{\varrho_{\rm LB}}} - 1\right] \approx 0.6\frac{d_b}{\tan\theta}\,; \tag{83}$$

here we have used the positive root for a physically meaningful result and the numerical values for the respective densities given in Sect. 3.1.

It has been implicitly assumed that the half opening angle θ will remain constant, i.e. $\tan\theta = R_j/L_j$, where R_j is the radius of the jet cross section at distance L_j. This is true, because the jet is still expanding freely until it hits the cloud, and the so-called working surface has not yet fully developed. It is known that in the case the ambient medium is constant (like here), the jet will reconfine (e.g. Sanders 1983; Falle 1991), in order to drive a bow shock into the ambient medium; however this is not relevant in the initial stage of expansion under consideration.

Since v_j is the maximum velocity, $\Delta t > t_{\rm exp}$, which is

$$t_{\rm exp} \sim \frac{L_j}{v_j} \approx 0.35\,\frac{d_b}{c_{\rm LI}\tan\theta}\,. \tag{84}$$

Adopting the values derived earlier for $B_{-6} = 5$, $d_b = 2.2\,{\rm pc}$, $T_{\rm LI} = 2.5\times10^6\,{\rm K}$ and $\tau_g = 4.9\times10^5\,{\rm yr}$, we can now conclude that the effect of accelerating the clouds by the plasma, which is streaming out of the holes and pushing the clouds, is of the same order as the initial acceleration given in Eq. (63), if the half opening angle satisfies

$$\begin{aligned}\tan\theta \;&\sim\; 2.3\frac{d_b}{\tau_g c_{\rm LI}} \qquad (85)\\ \Longrightarrow \theta \;&\sim\; 3.1^\circ\,,\end{aligned}$$

and $L_j \sim 11\,d_b \approx 24.2\,{\rm pc}$.

It is unlikely that such a well collimated jet exists in the present case, and the effect of accelerating the clouds by the plasma streaming out of the holes is probably rather small.

4. Comparison with observations

4.1. ROSAT PSPC X-ray data

Once blobs have formed and detached from the Local Bubble boundary, the remaining holes (or depressions, depending on the ratio of blob to wall extension) in the hydrogen distribution can cause corresponding changes in the absorption of soft X-rays from distant emission regions. This should be accompanied by spectral changes as softer X-rays are more heavily attenuated than harder X-rays.

The ideal data base for such an analysis of absorption and emission variation of soft X-rays is the ROSAT XRT/PSPC All-Sky Survey: sky maps of intensities and their uncertainties of the soft X-ray background (SXRB, 0.1–2.0 keV) have been produced in 7 energy bands with $12'$ spatial resolution (see Snowden et al. 1995, 1997, and references therein). These maps have been carefully cleaned from non-cosmic contaminations (e.g., particle events, scattered solar X-rays) and point sources have been masked. Also telescope vignetting and deadtime corrections have been applied.

The ROSAT survey maps of the Loop I region at low energies, primarily the R1 band (PSPC channels 8–19, $\sim$ 0.1–0.2 keV) indicate the presence of a coherent neutral gas sheet filling the interaction ring as found by EA95. Judging from the known optical depth in the R1 band the mean column density of this gas sheet is $\sim 10^{20}\,{\rm cm}^{-2}$, because it is blocking most of the R1 band radiation coming from behind.

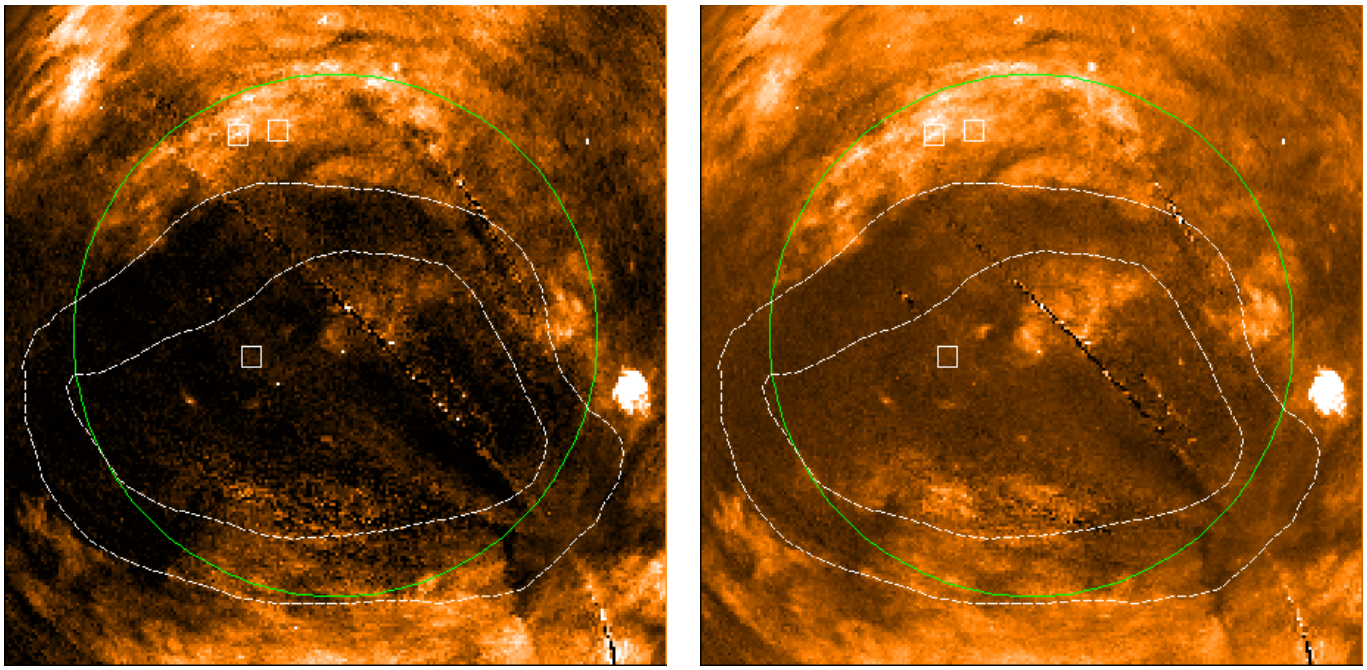

Fig. 5. ROSAT PSPC maps of the Loop I region in the R1 (left) and R2 (right) band centered on the centre of the radio continuum (RC) Loop I, $(l, b, r) = (330^\circ, +17.5^\circ, 58^\circ)$. Dashed white lines mark the contours of the HI ring formed by the interaction of Loop I with the LB as described in Egger & Aschenbach (1995). For details see text.

This can be seen in Fig. 5 which shows ROSAT survey maps of the Loop I region in the ROSAT R1 (left, ~ 0.08–0.28 keV) and R2 energy bands (right, ~ 0.15–0.28 keV). The green line is a $r = 58^\circ$ small circle fit to the radio continuum (RC) Loop I (Berkhuijsen 1972). The maps are centered on the centre of RC Loop I ($l = 330^\circ, b = 17.5^\circ$), galactic north is up. The dashed white lines mark the contours of the HI ring formed by the interaction of Loop I with the LB as described in Egger & Aschenbach (1995). The intensities of both images are scaled in a way that the regions outside (north) of the interaction zone appear to be equally bright. Hence, the intensity ranges are 0–820×10^{-6} counts s^{-1} arcmin^{-2} and 0–1300×10^{-6} counts s^{-1} arcmin^{-2} for R1 and R2, respectively. One can see that the interaction ring is casting equally deep shadows onto Loop I on both of the low energy images due to its high absorbing column density of $\sim 7 \times 10^{20}$ cm^{-2} which corresponds to $\tau > 4$ for both bands. Also the view through the ring into the interior of the Loop I superbubble is inhibited by intervening neutral gas. However, the absorption is stronger in R1 than in R2, which roughly corresponds to optical depth unity in R1 as will be shown below. This is clear evidence for the existence of a coherent neutral gas sheet or "wall" separating the LB from Loop I.

Quantification of the absorbing column density using the R2/R1 band ratio is not trivial since we also have to take into account a certain amount of foreground emission in both bands coming from the LB. To make a rough estimate we compare the mean intensities of three separate regions, each about $5^\circ \times 5^\circ$ in size, one of them inside and two outside the interaction zone. We will use the labels A, B and C for the upper left, the upper right and the lower box (drawn in the ROSAT images in Fig. 5, respectively. The three regions have been chosen such that the spectra of the background sources are roughly equal: $T_{\rm NorthPolarSpur} \approx T_{\rm centralLoop\ I} \approx 3 \times 10^6$ K. This precondition, however, is not very critical as will be shown below. Assuming now that the LB foreground emission $I_{\rm LB}$ is constant we obtain the following equations:

$$
\begin{aligned}
R1(A) &= R1_L + R1_S(A) = 518 \\
R1(B) &= R1_L + R1_S(B) = 486 \\
R1(C) &= R1_L + R1_S(C) = 189 \\
R2(A) &= R2_L + R2_S(A) = 868 \\
R2(B) &= R2_L + R2_S(B) = 785 \\
R2(C) &= R2_L + R2_S(C) = 246\ ,
\end{aligned}
$$

where $R1(A)$, $R1(B)$, $R1(C)$, $R2(A)$, $R2(B)$, and $R2(C)$ are the total median intensities within the three regions in the two energy bands in units of 10^{-6} counts s^{-1} arcmin^{-2}. $R1_L$ and $R2_L$ is the LB foreground emission, $R1_S(A)$, $R1_S(B)$, $R1_S(C)$, $R2_S(A)$, $R2_S(B)$, and $R2_S(C)$ are the absorbed background intensities for bands R1 and R2, respectively. In order to cancel the foreground we subtract:

$$
\begin{aligned}
R1(A) - R1(C) &= R1_S(A) - R1_S(C) \\
R1(B) - R1(C) &= R1_S(B) - R1_S(C) \\
R2(A) - R2(C) &= R2_S(A) - R2_S(C) \\
R2(B) - R2(C) &= R2_S(B) - R2_S(C)\ .
\end{aligned}
$$

Hence, we obtain the hardness ratios $\frac{R2(A)-R2(C)}{R1(A)-R1(C)} = 1.89$ and $\frac{R2(B)-R2(C)}{R1(B)-R1(C)} = 1.81$. Fig. 10a in Snowden et al. (1997) shows

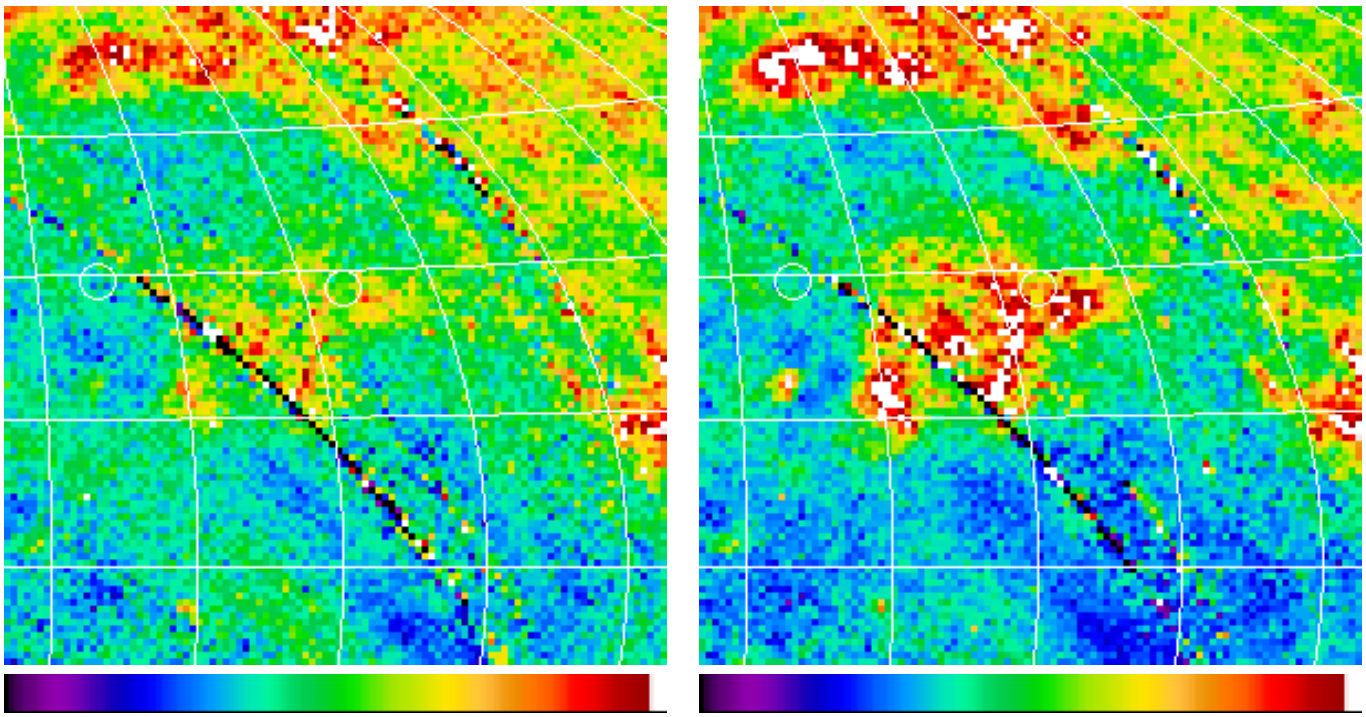

Fig. 6. ROSAT PSPC survey X-ray intensity maps of the central part of the Loop I region in the R1 (left, PSPC channels $8-19$, ~ 0.08–0.28 keV, dynamic range 0–450×10^{-6} counts s^{-1} arcmin^{-2}) and R2 (right, channels 20–41, ~ 0.15–0.28 keV, 0–650×10^{-6} counts s^{-1} arcmin^{-2}) band in galactic coordinates in Aitoff-Hammer projection. The pixel size is 40 arcmin. Coordinate lines are in steps of 15° starting at $l = 345^\circ$ (left) and $b = 0^\circ$ (bottom), the two regions with χ^2-contour grid analysis (Fig. 7) are indicated by circles (A1 right, A2 left). Errors in the band rates (R1, R2) in the selected regions (A1, A2) are less than 4% at the 1σ level while the difference between A1 (bright) and A2 (dark) exceeds 34%.

that for a R2/R1 ratio of 1.8–1.9 we get an absorbing column density of $N_{\rm H,wall} = 0.7$–0.8×10^{20} cm^{-2} assuming a thermal background emission of $\log T \approx 6.5$. This result is almost insensitive to variations in background temperature between $\log T = 6.2$–6.8. $N_{\rm H,wall} \sim 0.75 \times 10^{20}$ cm^{-2} is therefore a conservative value. If we assume that the line of sight through the LB is somewhat larger at higher galactic latitudes (fields A and B) than it is in the galactic plane (field C), as is indicated by some current models, then the R2/R1 contrast is even higher for the absorbed background sources. Another way to get a rough estimate for the wall column density is to use the model of Snowden et al. (1998) for the LB quantities for $R1_L + R2_L$ and $R2_L/R1_L$. For position C we would then obtain $R1_L = 156$ and $R2_L = 194$. With $R1(C) = 189$ and $R2(C) = 246$ the hardness ratio is $\frac{R2(C)-R2_L}{R1(C)-R1_L} \sim 1.6$. Using Fig. 10a of Snowden et al. (1997) this corresponds to $N_{\rm H} \sim 0.4 \times 10^{20}$ cm^{-2}. These numbers are obtained by hardness ratio analysis only, i.e. by analysis of only two bands, but are nevertheless sufficient to show X-ray evidence for the existence of a coherent (large-scale) neutral gas sheet between the Local Bubble and Loop I. In the next section we will show a more detailed spectral analysis. We want to note that in the first estimate statistical errors are negligible ($\sim 1\%$) but systematic errors may be stronger due to the separation of regions A and B from C and the assumed spectral constancy of the local and distant emission regions. In the second approach errors are difficult to obtain from Snowden et al. (1998) as this study aimed at a large-scale description of the local and distant 1/4 keV X-ray sky by smoothing filters and does not provide uncertainties for individual sky regions.

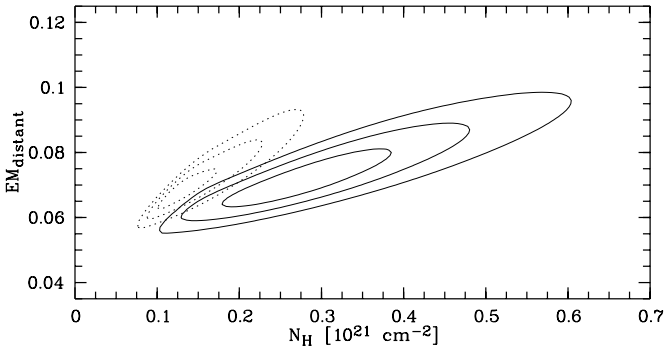

Fig. 7. χ^2 contour plots (1σ, 2σ, and 3σ) of the spectral fits for $EM_{\rm LI}$ and $N_{\rm H}$ for the two selected regions A1 (dashed) and A2 (solid contour lines). For details see text.

On smaller scales, however, there are several directions where the H I wall appears to be disrupted, which is indicated by X-ray enhancements and spectral variations in the R1 and R2 bands: The R1 band count rate is only slightly increased, the R2 band rate (channels 20–41), however, shows significantly higher values (see Fig. 6) as compared to surrounding regions.

This can be interpreted in terms of still considerable absorption for the soft R1 band X-rays, and beginning transparency for R2 band emission. In this region of enhanced X-ray intensity also a local minimum of the galactic neutral hydrogen column density is found. This supports the idea of blobs that have detached from the boundary and have left a remaining boundary with decreased density.

4.2. Spectral fits

Now we want to quantitatively examine the spectral variation visible in the R1 and R2 band. Since the ROSAT PSPC (as any proportional counter) has only a moderate energy resolution, the number of free spectral model parameters is limited to a maximum of 5. Our input model consists of three emission components (similar to Egger 1995). One is the extragalactic background, which we assume to follow a power-law spectrum with full galactic absorption derived from 21 cm maps. All parameters for this component are kept fixed during the fits but have been determined separately at high galactic latitudes. We have also included a local unabsorbed thermal component representing the Local (Hot) Bubble as Raymond-Smith plasma (in collisional ionization equilibrium), where the temperature $T_{\rm LB}$ was fixed to the canonical value of $kT_{\rm LB} = 0.10$ keV in agreement with other authors (e.g., Snowden et al. 1990, 1998; Egger 1995). The emission measure $EM_{\rm LB}$ is a free parameter since we allow for local intensity variations. The third component is due to distant thermal emission from the Loop I superbubble with free temperature $T_{\rm LI}$, emission measure $EM_{\rm LI}$, and foreground absorption $N_{\rm H}$ (which has an upper limit of less than 1.5 times the galactic value to account for uncertainties in the determination of the galactic $N_{\rm H}$). The values for the galactic neutral hydrogen column densities have been obtained by scaling the IRAS $100\,\mu$m map to data by Dickey & Lockman (1990), since the latter have only a spatial resolution of 2°. There is no gain in using a more complicated model because having 4 free parameters and 7 data points is close to the feasible limit of the χ^2 fit procedure.

The fits were performed for two regions inside the interaction ring (as defined by EA95), a bright area (A1) at $(l, b) = (311.1^\circ, +27.7^\circ)$ and a darker one (A2) at $(l, b) = (337.9^\circ, +28.9^\circ)$ (see Fig. 6). These regions were chosen to lie away from sky map portions with excessive background contamination to avoid effects of over- or undercorrections of these components (e.g., long-term X-ray enhancements) by the background cleaning processes. Cross-checking with the ROSAT Bright Source Catalog[4] (Voges et al. 1999) we convinced ourselves that the contribution by point sources was negligible. Moreover, we tried to avoid a bias due to the galactic bulge emission. Finally, the regions should not be separated too much to minimize variations of the distant emission component. Our selected areas A1 and A2 are otherwise typical regions and the restrictions have only been imposed in order to isolate the effects of absorption and spectral variation. The size of each region is 3×3 pixel of $40'$, i.e. ~ 4 square degrees. This corresponds to a diameter of the blobs of $\sim 1.6 \pm 1$ pc for a distance estimate of the wall of 40 ± 25 pc, which is in good agreement with the estimated sizes derived earlier.

The enhanced region A1 shows a deficiency of hydrogen by $1.4\,10^{20}$ cm^{-2} ($N_{\rm H}({\rm A1}) = 1.2^{+0.2}_{-0.1}\,10^{20}$ cm^{-2}, $N_{\rm H}({\rm A2}) = 2.6^{+0.6}_{-0.5}\,10^{20}$ cm^{-2}) compared to the neighbouring region without enhancement (A2). For both areas we derived a distant temperature of $kT_{\rm LI} = 0.20$ keV. In Fig. 7 we illustrate the significance of our results by χ^2 contour plots for both regions (A1 dashed, A2 solid) for parameters $N_{\rm H}$ (x-axis) and $EM_{\rm LI}$ (y-axis). Contour levels are 1σ, 2σ, and 3σ (from inside to outside). There are no significant changes in the properties of the distant thermal emission component (temperature, emission measure).

The column density contrast is of the order of the column density of the HI shell around Loop I ($\sim 10^{20}$ cm^{-2}, see e.g. Egger 1995) which is consistent with the view that most of the shell in the direction to the enhancement has been disrupted into blobs. Such blobs are not a rare event as will be shown in a separate paper (Freyberg et al. 2000), in which we report on the search for H I blobs in the data of the Leiden/Dwingeloo 21 cm survey. This suggests that a hydromagnetic instability is working on a larger scale.

4.3. Interstellar absorption lines

The existence of a wall is not only supported by X-ray spectral analysis, but also by independent interstellar absorption line measurements. EA95 and Egger (1998) have shown that there is a distinct rise in the H I column densities of stars in the direction towards the ring between the Local Bubble and Loop I. At a distance of about 70 pc, $N_{\rm H}$ jumps from $< 1 \times 10^{20}$ cm^{-2} to $> 7 \times 10^{20}$ cm^{-2}. We have reanalyzed the absorption data compiled by Fruscione et al. (1994) by using recent HIPPARCOS distances. The result is shown in Fig. 8, corresponding to Fig. 3 of Egger (1998). The left panel summarizes for which sample stars HIPPARCOS data are available (filled symbols), and whether these are "close" (triangles) or "distant" (squares) with respect to a distance of ~ 80 pc. The right panel still shows a distinct rise in $N_{\rm H}$, at a somewhat larger distance as some stars are now slightly further away. However, the main conclusion, namely the existence of an interaction ring, is still clearly visible.

In principle all the stars with $N_{\rm H} > 10^{20}$ cm^{-2} could be located at large distances even far behind the Loop I. However, we have checked that more than half of the 40 stars in the direction of the ring are located within 140 pc from the Sun. There are 6 stars between 89 and 140 pc with $10^{20.5} < N_{\rm H} < 10^{21.15}$ cm^{-2}, and one star at 130 pc with $N_{\rm H} = 10^{19.8}$ cm^{-2} (however, this star is located in the direction of the H I enhancements of the ring). We further emphasize that all stars at $d > 140$ pc have $N_{\rm H} < 10^{21.23}$ cm^{-2}, i.e. at the same level as before. Therefore we conclude that the HI enhancement cannot be due to neutral hydrogen beyond Loop I and the jump in $N_{\rm H}$ should be interpreted as a dense absorbing ring. As Loop I is a superbub-

[4] Electronically available at
http://www.rosat.mpe-garching.mpg.de/survey/rass-bsc/

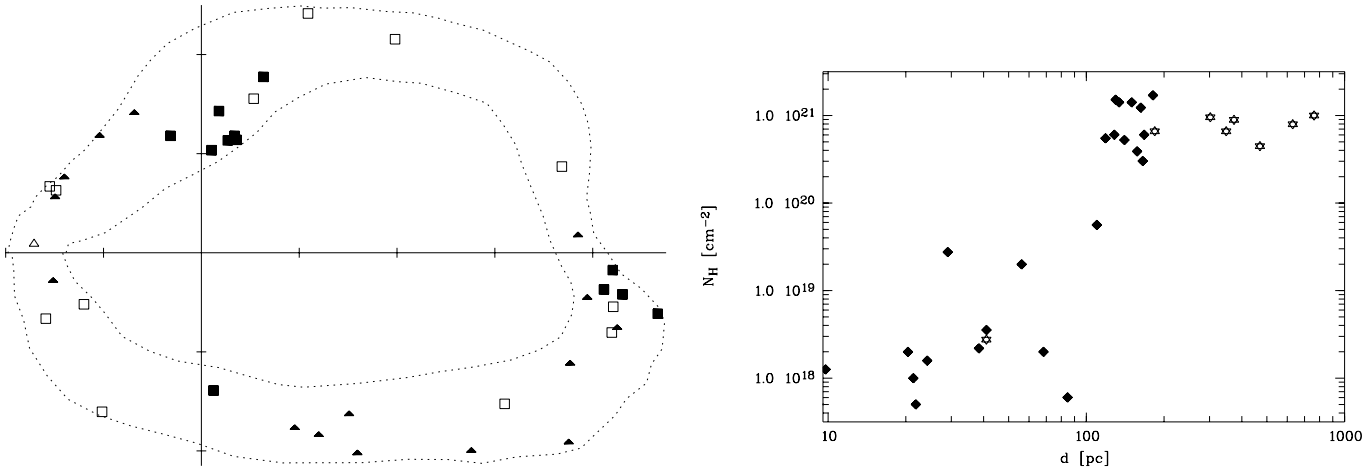

Fig. 8. *Left:* Positions of stars projected onto the annular X-ray shadow cast by the interaction ring. Filled symbols (triangles: $d < 80$ pc, squares: $d > 80$ pc) denote stars with HIPPARCOS distances while open symbols represent stars without these new distances. The galactic plane ($b = 0°$) as well as the center ($l = 0°$) are indicated with tics at each $20°$. *Right:* H I column densities towards stars projected onto the interaction ring, again filled symbols stand for stars with HIPPARCOS distances and empty symbols for stars without. Clearly, $N_{\rm H}$ rises to $\sim 7 \times 10^{20}$ cm^{-2} at around 100 pc. Absorption data taken from Fruscione et al. (1994).

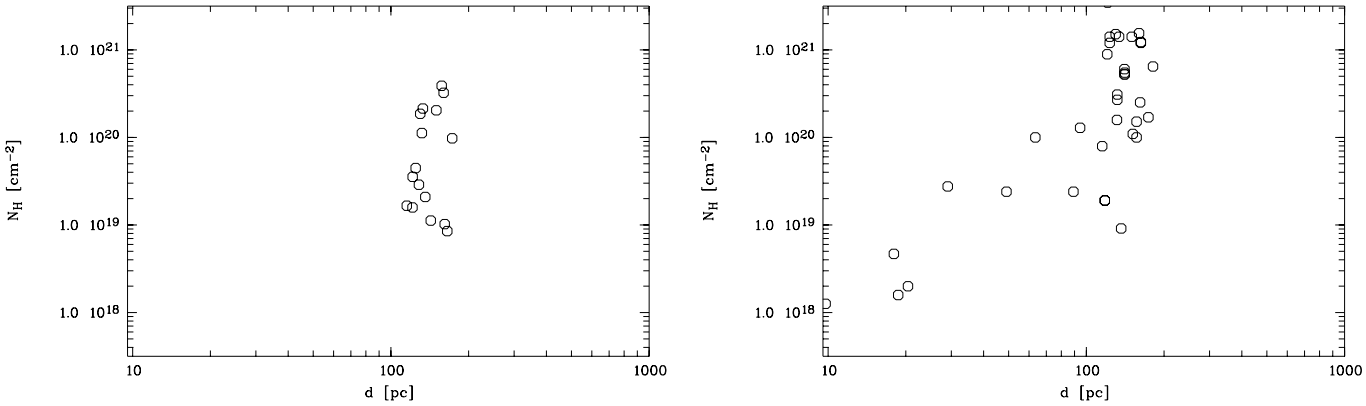

Fig. 9. H I column densities of stars in the direction of the ring *and* towards the wall with $b > 5°$ as a function of HIPPARCOS distances. *Left:* $N_{\rm H}$ derived from Na I absorption measurements. *Right:* $N_{\rm H}$ derived from all other methods (e.g., Ly α, Mg II, EUV). The rise in column density to $N_{\rm H} \sim 10^{20}$ cm^{-2} occurs at a distance of $\gtrsim 60$ pc, thus indicating the existence of a wall. H I column densities derived from Na I appear to be lower, the sampling in distance is not as complete as in the right panel. Absorption data taken from Fruscione et al. (1994).

ble with ongoing star formation in which gas is continuously heated it is a valid assumption that the pressure is higher than in the adjacent Local Bubble where no evidence for an active stellar cluster is found. Therefore the interaction shell (wall) is pushed towards the Local Bubble with respect to the ring. Thus the distance of $\sim$ 80–100 pc to the ring may serve as an upper limit for the distance to the wall, while parts near the centre direction of Loop I may be closer.

The compilation by Fruscione et al. (1994) contains column densities derived by various methods. We have analyzed a subsample of stars with directions towards the ring and towards the wall inside the ring with $b > 5°$ (our X-ray analysis was restricted to this range as well). In the left panel of Fig. 9 we have shown the absorption-distance-relation derived from Na I measurements, whereas in the right panel this relation derived from all other methods (like Ly α, Mg II, EUV,...) is displayed. The Na I absorption column densities tend to be systematically below the ones obtained by other methods. This may be possibly due to ionization and/or abundances effects which influence the conversion factor of Na I to H I. The conversion factor by itself is a source of error in contrast to methods evaluating hydrogen directly (e.g., Ly α), and the correlation between $N_{\rm NaI}$ and $N_{\rm HI}$ shows considerable scatter (one order of magnitude) (cf. Ferlet et al. 1985). Diamond et al. (1995) have used Na I absorption line studies to map the distribution of interstellar matter. Only two stars of their sample are in our field of interest (numbers 46 and 47 of their Table 3) and both are not in conflict with our model of a wall inside an interaction ring.

In the recent literature the Na I method is extensively described e.g. by Welsh et al. (1998). Unfortunately in the wall region, for a distance less or equal 100 pc, there are not many background stars with measured Na I column densities avail-

able. Therefore Welsh et al. conclude that it is difficult to derive the detailed morphology of the LISM using Na I absorption measurements.

5. Discussion and conclusions

The mechanism of producing HI clouds by a hydromagnetic Rayleigh-Taylor instability is operating under quite general conditions, provided there exists a pressure imbalance between the two interacting bubbles. Therefore the assumption of collisional ionization equilibrium (CIE) is not critical. It has been shown that non-equilibrium ionization models of the Local Bubble can explain a number of features that are problematic in standard CIE models (Breitschwerdt & Schmutzler 1994; Breitschwerdt 1996). The pressure in the Local Bubble is typically a factor of 4–5 lower in these models. It is therefore in equilibrium with the local clouds, and thus guarantees their existence in the long run.

There are a number of competing instabilities that could in principle occur. Kelvin-Helmholtz instabilities depend on the systematic velocity difference in adjacent regions. Considerable deviations from spherical symmetry would be necessary in order to produce a significant difference between the velocity in the shell and the hot bubbles, respectively. Moreover it has been shown by Kahn (1980) in the case of a stellar wind, that second order effects limit the growth rate substantially.

Thin shells, held under pressure by shocks like in accretion flows are susceptible to "thin shell" or "bending mode" instabilities (e.g. Vishniac 1993). This effect is mainly due to a separation of net momentum of the incoming flow from both sides, depositing, say positive momentum in the upward and negative momentum in the downward flow, thereby increasing any existing "ripples". While these calculations do not consider any magnetic field, which would inhibit instability by tension forces, it can be estimated that the typical inverse growth time for the unmagnetized case is of the order $\tau_g^{-1} \sim c_{\rm sh} k \sqrt{z_m/\delta R_{\rm sh}}$, where $c_{\rm sh}$ is the speed of sound in the shell, k the wavenumber and z_m the mean (density weighted) position, defined by $z_m = \int_{z1}^{z2} z\varrho dz / \int_{z1}^{z2} \varrho dz$. In our case this amounts to about the sound crossing time for unstable wavelengths of the order $\delta R_{\rm sh}$ in the shell, $\tau_g \sim \delta R_{\rm sh}/c_{\rm sh} \approx 4 \times 10^{13}$ s. Introducing a magnetic field would certainly make it larger than the value we derived for the hydromagnetic Rayleigh-Taylor instability.

In a subsequent paper (Freyberg et al., 2000) we will show that our proposed mechanism can indeed be responsible for a swarm of neutral clouds, drifting from Loop I towards the anticenter direction, which we have found in the Leiden-Dwingeloo 21 cm Survey by a newly developed cloud detection algorithm.

If the Local Bubble has a temperature as high as $\sim 10^6$ K, there exists a temperature gradient of 2 orders of magnitude at the interface between a cloud and the bubble plasma. Due to their high mobility, thermal electrons will deposit energy in the warm cloud and thus cause the gas to evaporate. The timescale is estimated to be about $2.3 \times 10^4\, R_{\rm pc}$ yr (Egger et al. 1996), which is short compared to the travel time of the blobs in the hot medium. However, we have shown that, as a result of their generation, the clouds are magnetized, with the magnetic field being most likely parallel to the surface. There is no hint that this field is strongly turbulent on scales much smaller than the cloud size, and hence heat conduction may be efficiently suppressed.

When the blobs travel through the Local Bubble from their place of birth to the solar neighbourhood, they might be subject to ablation. However, the low density in the Local Bubble ensures that the column of mass that is encountered is roughly two orders of magnitude smaller than that of the cloud, and therefore ablation is negligible.

Soft X-rays (below 0.4 keV) are quite sensitive to absorption variations due to the strong energy dependence of the photoelectric absorption cross sections. Therefore searching for variations in band ratio maps is a powerful tool to look for candidates for Rayleigh-Taylor instability "holes" (drastically locally reduced thickness of the wall). These spectral variations may, however, also be caused by intrinsic emission variations such as different temperatures. Therefore special care has been taken to eliminate as many effects as possible that might bias the analysis. Point sources have been subtracted. The sky maps have been thoroughly cleaned from non-cosmic background components. Galactic bulge intensity variations were reduced by selection on galactic latitude. There is no substantial temperature gradient to be expected in the diffusely emitting plasma of the Loop I superbubble on scales of 20° (~ 20 pc) since it would be wiped out by pressure waves within the order of a few 10^4 years. Hence the method is excellent for probing absorbers and holes in the interaction zone. Spectral fits using 7 energy bands with a simple but realistic model have indeed shown that the emission parameters do not change, but only the absorption between the Local Bubble and the more distant thermal component.

In conclusion we have presented evidence that the scenario of small compact cloudlets expelled from the bubble interaction zone by Rayleigh-Taylor instabilities is a convincing explanation for the presence of partially neutral clouds in a fully ionized LISM. Also the general flow of the clouds (direction) and the magnitude of the velocity, in particular the LIC, towards the anticenter direction is naturally explained.

Finally one could ask how rare an event like the interaction of bubbles would be, in order to infer the relevance of the proposed mechanism in interstellar space in general. From radio observations (Quigley & Haslam 1965) it is known that there are four almost circular rings projected onto the sky and appropriately termed Radio Loops I to IV, which are probably old superbubbles or supernova remnants. Their apparent sizes suggest that they are very close by, and interaction at some stage during their evolution is not unlikely. Moreover, there are a number of well-known examples of nearby bubbles: Eridanus (distance $D \sim 100$–150 pc), Gum Nebula ($D \sim 200$–250 pc), Orion ($D \sim 450$ pc) and Monogem Ring ($D \sim 100$–1300 pc). The tendency of bubbles to cluster is straightforward to understand, if we take into account that star forming regions are not homogeneously spread over the galactic disk, but concentrate in spiral arms. Images of extragalactic HII regions demonstrate this behaviour quite convincingly. We therefore expect that the interaction of bubbles does occur in several places in the Galaxy,

and may generally be responsible for mixing in neutral clouds from interaction regions into the hot interior of active and extinct interstellar bubbles.

Acknowledgements. We thank Franz Kahn†, who stimulated this work, for fruitful discussions. We also wish to thank Gregor Morfill for many helpful comments on the manuscript. DB is grateful to J. Trümper and the MPI für Extraterrestrische Physik, where most of this work was done, for excellent working conditions. He also thanks his colleagues Bruce Draine, Edward Jenkins and Russell Kulsrud at the Department of Astrophysical Sciences for interesting discussions, and Scott Tremaine and Princeton University, where this work was completed, for their hospitality. DB acknowledges support from the Deutsche Forschungsgemeinschaft (DFG) by a Heisenberg fellowship. The ROSAT project is supported by the German Bundesministerium für Bildung, Wissenschaft, Forschung und Technologie (BMBF/DLR) and the Max-Planck-Gesellschaft (MPG).

Appendix A: the fastest growing mode

The most unstable wavenumber, k_*, can be found from Eq. (49) by applying the necessary and sufficient conditions for $\omega(k)$:

$$\text{(i)} \quad \frac{d\omega}{dk} = 0$$

$$\text{(ii)} \quad \left[\frac{d^2\omega}{dk^2}\right]_{k=k_*} < 0\,.$$

The first condition yields

$$\begin{aligned}\frac{d\omega}{dk} &= \frac{1}{2}\left[g_0 k\frac{\varrho_2-\varrho_1}{\varrho_2+\varrho_1} - \frac{k^2\cos^2\alpha}{4\pi}\frac{\left(B_{0,1}^2+B_{0,2}^2\right)}{\varrho_1+\varrho_2}\right]^{-(1/2)} \times \\ &\times \left\{g_0\frac{\varrho_2-\varrho_1}{\varrho_2+\varrho_1} - \frac{k\cos^2\alpha}{2\pi}\frac{\left(B_{0,1}^2+B_{0,2}^2\right)}{\varrho_1+\varrho_2}\right\} \qquad \text{(A.1)} \\ &= 0\end{aligned}$$

and therefore

$$\Longrightarrow k_* = \frac{2\pi g_0(\varrho_2-\varrho_1)}{\left(B_{0,1}^2+B_{0,2}^2\right)\cos^2\alpha}\,. \qquad \text{(A.2)}$$

Condition (ii) requires

$$\begin{aligned}&-\frac{1}{4}\left[...\right]^{-(3/2)}\left\{...\right\}^2 \\ &+\frac{1}{2}\left[...\right]^{-(1/2)}\left(-\frac{\cos^2\alpha}{2\pi}\frac{\left(B_{0,1}^2+B_{0,2}^2\right)}{\varrho_1+\varrho_2}\right) < 0\,, \qquad \text{(A.3)}\end{aligned}$$

where $[...]$ and $\{...\}$ are shorthand for the expressions in square and curly brackets in Eq. (A.1).

In Eq. (A.3) the term in curly brackets vanishes for $k = k_*$ and the term in square brackets is $\propto \omega^2$ which is real and positive for $k < k_c$. The term in round brackets is always negative and hence $\left(d^2\omega/dk^2\right)_{k=k_*} < 0$.

References

Berkhuijsen E.M., Haslam C.G.T., Salter C.J., 1971, A&A 14, 252
Bochkarev N.G., 1987, Ap&SS 138, 229
Breitschwerdt D., 1996, Space Sci. Rev. 78, 173
Breitschwerdt D., Schmutzler T., 1994, Nat 371, 774
Centurion M., Vladilo G., 1991, ApJ 372, 494
Cox D.P., Anderson P.R., 1982, ApJ 253, 268
Cox D.P., 1998, In: Breitschwerdt D., Freyberg M.J., Trümper J. (eds.) Proceedings of the IAU Colloquium No. 166, The Local Bubble and Beyond. Lecture Notes in Physics 506, p. 121
Courant R., Friedrichs K.O., 1948, Supersonic Flow and Shock Waves. Interscience, New York
Diamond C.J., Jewell S.J., Ponman T.J., 1995, MNRAS 274, 589
Dickey J.M., Lockman F.J., 1990, ARA&A 28, 215
Dring A.R., Linsky J., Murthy J., et al., 1997, ApJ 488, 760
Egger R.J., 1993, Ph.D. Thesis, TU München, MPE Report 249
Egger R.J., 1995, In: Ferrara A., McKee C.F., Heiles C., Shapiro P. (eds.) The Physics of the interstellar medium and the intergalactic medium. ASP Conf. Ser. 80, p. 45
Egger R.J., 1998, In: Breitschwerdt D., Freyberg M.J., Trümper J. (eds.) Proceedings of the IAU Colloquium No. 166, The Local Bubble and Beyond. Lecture Notes in Physics 506, p. 287
Egger R.J., Aschenbach B., 1995, A&A 294, L25 (EA95)
Egger R.J., Freyberg M.J., Morfill G.E., 1996, Space Sci. Rev. 75, 511
Falle S.A.E.G., 1991, MNRAS 250, 581
Ferlet R., Vidal-Madjar A., Gry C., 1985, ApJ 298, 838
Freyberg M.J., Breitschwerdt D., Egger R., 2000, A&A (in preparation)
Frisch P.C., 1995, Space Sci. Rev. 72, 499
Frisch P.C., 1996, Space Sci. Rev. 78, 213
Frisch P.C., et al., 1999, ApJ 525, 492
Fruscione A., Hawkins I., Jelinsky P., Wiecigroch A., 1994, ApJS 94, 127
Innes D.E., Hartquist T.W., 1984, MNRAS 209, 7
Jakobsen P., Kahn S.M., 1986, ApJ 309, 682
Kahn F.D., 1980, A&A 83, 303
Lallement R., 1998, In: Breitschwerdt D., Freyberg M.J., Trümper J. (eds.) Proceedings of the IAU Colloquium No. 166, The Local Bubble and Beyond. Lecture Notes in Physics 506, p. 19
Lallement R., Bertin P., Ferlet R., Vidal-Madjar A., Bertaux J.L., 1994, A&A 286, 898
Lallement R., Ferlet R., 1997, A&A 324, 1105
Lazarian, A. Vishniac, E., 2000, In: Arthur J., Brickhouse N., Franco J. (eds.) Proceedings of the conference Astrophysical Plasmas: Codes, Models, and Observations. Revista Mexicana de Astronomía y Astrofísica vol. 9, p. 55
Linsky J.L., 1996, Space Sci. Rev. 78, 157
Linsky J.L., Redfield S., 1999, BAAS 31(3), 890
McKee C.F., Ostriker J.P., 1977, ApJ 218, 148
Petschek H.E., 1964, In: Hess W.N. (ed.) AAS-NASA Symposium, SP-50, US Government Printing Office, p. 425
Quigley M.J.S., Haslam C.G.T., 1965, Nat 208, 741
Raymond J.C., Smith B.W., 1977, ApJS 35, 419
Sanders R.H., 1983, ApJ 266, 73
Slavin J.D., Frisch P.C., 1998, 305
Smith R.K., Cox D.P., 1998, In: Breitschwerdt D., Freyberg M.J., Trümper J. (eds.) Proceedings of the IAU Colloquium No. 166, The Local Bubble and Beyond. Lecture Notes in Physics 506, p. 133
Snowden S.L., 1998, In: Breitschwerdt D., Freyberg M.J., Trümper J. (eds.) Proceedings of the IAU Colloquium No. 166, The Local Bubble and Beyond. Lecture Notes in Physics 506, p. 103

Snowden S.L., Cox D.P., McCammon D., Sanders W.T., 1990, ApJ 354, 211
Snowden S.L., Egger R., Finkbeiner D.P., Freyberg M.J., Plucinsky P.P., 1998, ApJ 493, 715
Snowden S.L., Egger R., Freyberg M.J., et al., 1997, ApJ 485, 125
Snowden S.L., Freyberg M.J., Plucinsky P.P., et al., 1995, ApJ 454, 643
Spitzer L., 1978, In: Physical Processes in the Interstellar Medium. John Wiley & Sons, New York
Tomisaka K., Ikeuchi S., 1983, PASJ 35, 187
Vishniac E.T., 1993, ApJ 428, 186
Voges W., Aschenbach B., Boller Th., et al., 1999, A&A 349, 389
Warwick R.S., Barber C.R., Hodgkin S.T., Pye J.P., 1993, MNRAS 262, 289
Welsh B.Y., Crifo F., Lallement R., 1998, A&A 333, 101
Witte M., Banaskievicz M., Rosenbauer H., 1996, Space Sci. Rev. 78, 289
Yoshioka S., Ikeuchi S., 1990, ApJ 360, 352